

University of Denver

Digital Commons @ DU

---

Electronic Theses and Dissertations

Graduate Studies

---

1-1-2014

## Design and Evaluation of a Propulsion System for Small, Compact, Low-Speed Maneuvering Underwater Vehicles

Florence M. Mbithi  
*University of Denver*

Follow this and additional works at: <https://digitalcommons.du.edu/etd>



Part of the [Electrical and Computer Engineering Commons](#), [Mechanical Engineering Commons](#), and the [Propulsion and Power Commons](#)

---

### Recommended Citation

Mbithi, Florence M., "Design and Evaluation of a Propulsion System for Small, Compact, Low-Speed Maneuvering Underwater Vehicles" (2014). *Electronic Theses and Dissertations*. 414.  
<https://digitalcommons.du.edu/etd/414>

This Thesis is brought to you for free and open access by the Graduate Studies at Digital Commons @ DU. It has been accepted for inclusion in Electronic Theses and Dissertations by an authorized administrator of Digital Commons @ DU. For more information, please contact [jennifer.cox@du.edu](mailto:jennifer.cox@du.edu), [dig-commons@du.edu](mailto:dig-commons@du.edu).

DESIGN AND EVALUATION OF A PROPULSION SYSTEM FOR SMALL,  
COMPACT, LOW-SPEED MANEUVERING UNDERWATER VEHICLES

---

A Thesis

Presented to

the Faculty of the Daniel Felix Ritchie School of Engineering and Computer Science

University of Denver

---

In Partial Fulfillment

of the Requirements for the Degree

Master of Science

---

by

Florence M. Mbithi

March 2014

Advisor: Matthew J. Rutherford, Ph.D.

Author: Florence M. Mbithi  
Title: DESIGN AND EVALUATION OF A PROPULSION SYSTEM FOR SMALL,  
COMPACT, LOW-SPEED MANEUVERING UNDERWATER VEHICLES  
Advisor: Matthew J. Rutherford, Ph.D.  
Degree Date: March 2014

### **Abstract**

Underwater vehicles used to perform precision inspection and non-destructive evaluation in tightly constrained or delicate underwater environments must be small, have low-speed maneuverability and a smooth streamlined outer shape with no appendages. In this thesis, the design and analysis of a new propulsion system for such underwater vehicles is presented. It consists primarily of a syringe and a plunger driven by a linear actuator and uses different inflow and outflow nozzles to provide continuous propulsive force. A prototype of the proposed propulsion mechanism is built and tested. The practical utility and potential efficacy of the system is demonstrated and assessed via direct thrust measurement experiments and by use of an initial proof-of-concept test vehicle. Experiments are performed to enable the evaluation and modelling of the thrust output of the mechanism as well as the speed capability of a vehicle employing the propulsion system.

## **Acknowledgements**

I would like to offer my sincere appreciation to all those at the University of Denver who facilitated the successful completion of this work. Many thanks to my advisors Dr. Matthew Rutherford, Dr. Kimon Valavanis and Dr. Nikos Vitzilaios for their keen counsel throughout the course this work. I would also like to thank Dr. Jennifer Hoffman and Dr. Mohammad Mahoor for their support. I extend my thanks to my colleagues and friends at DU<sup>2</sup>SRI who all played a part in making this research a success.

In addition, I am very grateful to Trisha Litz for her support and guidance all through my degree. Much gratitude also to the University of Nairobi, Kenya and the AAHEP group for the assistance granted me during the course of my program. Finally, special thanks to my family and friends whose abundant love, prayers and encouragement throughout made the successful completion of my degree possible.

## Table of Contents

<b>Chapter 1: INTRODUCTION .....</b>	<b>1</b>
1.1    MOTIVATION .....	1
1.2    BACKGROUND .....	2
1.3    APPLICATIONS .....	3
1.4    PROBLEM STATEMENT .....	3
1.5    CONTRIBUTIONS .....	4
1.6    THESIS ORGANIZATION.....	4
<b>Chapter 2: LITERATURE REVIEW .....</b>	<b>6</b>
2.1    CONVENTIONAL PROPELLER-DRIVEN AUVs.....	6
2.1.1    PHOENIX AUV - NPS .....	6
2.1.2    THE REMUS 100 AUV .....	8
2.2    BIOMIMETIC AUVs .....	12
2.3    PROPULSION SYSTEMS FOR LOW-SPEED MANEUVERING AUVs .....	16
2.3.1    SYNTHETIC VORTEX-RING JET THRUSTERS .....	16
2.3.2    THE COANDA JET DEVICE.....	18
<b>Chapter 3: THE SYRINGE-PLUNGER PROPULSION MECHANISM .....</b>	<b>22</b>
3.1    OVERVIEW .....	22
3.2    DIRECT THRUST MEASUREMENT EXPERIMENTS .....	24
3.2.1    EXPERIMENTAL SETUP 1 .....	25
3.2.2    EXPERIMENTAL SETUP 2 .....	28
3.3    FORCE MODEL .....	30
3.4    EXPERIMENTAL RESULTS AND DISCUSSION .....	32
<b>Chapter 4: TEST VEHICLE MODELLING .....</b>	<b>39</b>
4.1    TEST VEHICLE DESIGN .....	39
4.2    TEST VEHICLE KINEMATICS AND DYNAMICS .....	41
4.2.1    ASSUMPTIONS .....	41
4.2.2    EQUATIONS OF MOTION .....	41
4.2.3    EXTERNAL FORCES AND MOMENTS ON VEHICLE .....	43
4.2.4    HORIZONTAL PLANE SIMPLICATIONS.....	45
4.3    LINEARIZATION OF THE MATHEMATICAL MODEL .....	47
<b>Chapter 5: TEST VEHICLE EXPERIMENTS .....</b>	<b>50</b>
5.1    EXPERIMENTAL SETUP.....	50
5.1.2    VEHICLE APPARATUS OPERATION.....	51
5.1.1    VEHICLE APPARATUS COMPONENTS AND SOFTWARE ..	53
5.2    VEHICLE APPARATUS AS A MECHATRONIC SYSTEM.....	54
5.2.1    THE MECHANICAL SUBSYSTEM.....	54
5.2.2    THE ELECTRICAL SUBSYSTEM .....	58
5.2.3    THE SOFTWARE AND COMMUNICATION SUBSYSTEM ..	61

<b>Chapter 6: TEST VEHICLE EXPERIMENTAL AND SIMULATION RESULTS</b>	<b>64</b>
6.1 DATA ANALYSIS .....	67
<b>Chapter 7: CONCLUSIONS AND RECOMMENDATIONS .....</b>	<b>85</b>
7.1 CONCLUSIONS.....	85
7.2 RECOMMENDATIONS FOR FUTURE WORK .....	86
<b>REFERENCES.....</b>	<b>88</b>

## List of Figures

Figure. 2.1: NPS Phoenix AUV .....	7
Figure. 2.2: REMUS 100 AUV.....	9
Figure. 2.3: REMUS 100 AUV standard configuration and sensors .....	9
Figure. 2.4: Biomimetic model prototype of the Octopus Vulgaris .....	13
Figure. 2.5: Schematic of a soft biomimetic micro-robotic fish .....	14
Figure. 2.6: The boxfish prototype .....	15
Figure. 2.7: An illustration of synthetic jet actuator operation .....	16
Figure. 2.8: An illustration of the basic coanda jet device shape and geometry.....	18
Figure. 2.9: Nested coanda jet device actuator and first generation prototype AUV .....	20
Figure. 2.10: Second generation prototype AUV: CJD system imbedded into the hull of the vehicle .....	20
Figure 3.1: Schematic illustration of the proposed syringe-plunger propulsion system...	22
Figure 3.2: Travelling-screw and Travelling-nut linear actuators .....	23
Figure 3.3: Schematic illustration of experimental setup 1 .....	25
Figure 3.4: An illustration of experimental setup 1 .....	26
Figure 3.5: An illustration of the actuator housing parts .....	27
Figure 3.6: The FSR sensor, FFP sensor and FC22 Load cell.....	27
Figure 3.7: Schematic illustration of experimental setup 2 .....	28
Figure 3.8: Normally-closed solenoid valve and 5V TTL relays .....	29
Figure 3.9: Schematic of the free body force diagram for setup 1 experiments. ....	30
Figure 3.10: Schematic of the free body force diagram for setup 2 experiments. ....	32

Figure 3.11: Experimental Setup 1: Net Thrust Output Results .....	34
Figure 3.12: Experimental Setup 2: Net Thrust Output Results .....	34
Figure 4.1: An illustration of the test vehicle shape and coordinate system.....	40
Figure 4.2: A solid model illustration of the first generation test vehicle .....	40
Figure 5.1: Test vehicle apparatus .....	50
Figure 5.2: Free body force diagram for the experiments with the test vehicle .....	51
Figure 5.3: The test vehicle in the water tank (full view).....	53
Figure 5.4: Test vehicle SolidWorks designs, Versions 1 and 2 .....	55
Figure 5.5: Initial apparatus .....	56
Figure 5.6: Plunger SolidWorks designs, Versions 1 – 3 .....	57
Figure 5.7: A schematic of the apparatus electrical circuit.....	58
Figure 5.8: Single-side stable TTL relays and Sparkfun Beefcake Relay Control Kit.....	59
Figure 5.9: Pololu DRV8825 and Probotix Stepper Motor Drivers .....	60
Figure 5.10: XK-1A board and XTAG-2 debug adapter .....	62
Figure 5.11: Sparkfun WiFly GSX Wi-fi module and user interface .....	63
Figure 5.12: Parallax PING))) <sup>TM</sup> Ultrasonic Distance Sensor .....	63
Figure 6.1: Experimental results: Average vehicle Position vs. Time plots.....	66
Figure 6.2: Average vehicle Position and Velocity plots: Plunger speed = 2.085cm/s for both Upstroke and Downstroke .....	67



Figure 6.3: Vehicle velocity curve (smoothed): Plunger speed = 2.085cm/s for both Upstroke and Downstroke.....	68
Figure 6.4: SIMULINK Non-linear test vehicle dynamics model.....	70
Figure 6.5: Constant Force Model: Position and Velocity profiles: Plunger speed = 2.085cm/s for both Upstroke and Downstroke .....	70
Figure 6.6: CASE 1: Constant Force Model: Position and Velocity profiles .....	72
Figure 6.7: CASE 2: Constant Force Model: Position and Velocity profiles .....	76
Figure 6.8: CASE 3: Constant Force Model: Position and Velocity profiles .....	79
Figure 6.9(a): Constant Thrust Output Results .....	82
Figure 6.9(b): Vehicle Speed Results .....	82

## **CHAPTER 1: INTRODUCTION**

The focus of this thesis is the design and evaluation of a novel propulsion system suitable for small, compact, low-speed maneuvering underwater vehicles. Interest in underwater robotic vehicles has grown drastically over the past couple of decades and autonomous underwater vehicles have proven to be extremely useful in marine science, ecology and other fields [1]–[4]. Underwater robots have been used for a range of important tasks such as deep sea exploration of natural resources and ship wreckage, inspection of offshore oil and gas platforms, evaluation of disaster sites and inspection of infrastructure [5]–[7]. This chapter discusses the motivation and background behind this research in propulsion systems for small underwater robotic vehicles.

### **1.1 MOTIVATION**

While there has been successful research into the conventional torpedo shaped underwater vehicles that have control surfaces such as fins, wings or rudders and use propeller-type thrusters, these vehicles are typically designed for high operating speeds and long-distance travel [2], [8]–[10]. Precision maneuvering, inspection and non-destructive evaluation of complex underwater environments is an increasingly important area of underwater robotics research and is complicated by the need for low speeds and small forces to correct minor deviations [1], [2], [9].

For this type of application, small, low-speed, highly maneuverable, compact AUVs that have smooth streamlined body shapes and no appendages are required. It

follows therefore that the propulsion systems employed for this specific class of underwater vehicles must be capable of providing low thrust, enable low-speed (1 – 10cm/s) precise maneuverability in multiple degrees of freedom and allow for embedding in the body of the vehicle and a smooth streamlined outer shape with no appendages [1], [2], [5].

## **1.2 BACKGROUND**

The conventional torpedo shaped underwater vehicles are typically powered by rotating propellers. Propeller-type thrusters have nonlinear effects which become more pronounced at low operating speeds [8], [9]. Control surfaces such as rudders or fins rely on forward velocity to provide forces and moments and do not function well if the vehicle is at low speed or stationary because the hydrodynamic forces they impose scale with the vehicle velocity squared [1].

Also, some propeller thrusters are asymmetric, meaning that they operate differently when reversed, which can complicate control when the propeller is commanded to provide a force that is changing direction frequently [9]. A common approach is to use multiple propellers to achieve better low-speed maneuvering and control. However, these designs sacrifice the low body volume and drag design and complicate control by not responding to short signals sent to the thrusters for accurate positioning [1], [2].

Additionally, there exist biologically-inspired underwater vehicles, Biomimetic Autonomous Underwater Vehicles (BAUVs), designed to mimic the propulsive capabilities and swimming mechanisms of fish and other underwater creatures. The biological study of underwater creatures offers inspiration for BAUV designs achieving

energy efficiency, stealth and maneuverability [3]. In this regard, the functionality of the biological source of inspiration is imitated by robot/vehicle designs relying on standard mechanical principles assembled in an unconventional manner.

Although maneuverability is an important requirement for many types of underwater inspection vehicles, it is particularly crucial for precision inspection tasks in tightly constrained environments [1], [2]. Control surfaces, thrusters, fins and other appendages protruding from the vehicle body can get tangled or damaged when attempting to access and traverse confined spaces. Hence propulsion mechanisms that allow for compact, tangle-free vehicle body shapes with minimal appendages are a desirable design approach for this class of applications. Finally, tethering of these underwater vehicles interferes with the dynamics of the vehicles and limits their accessibility and control fidelity.

### **1.3 APPLICATIONS**

The applications of AUVs using propulsion systems/mechanisms designed for low-speed maneuvering underwater vehicles include: external and internal Non-Destructive Evaluation (NDE) and inspection of water/fluid-filled piping systems of nuclear reactors, water treatment plants, chemical plants and offshore oil and gas platforms; and detailed small scale surveying, monitoring and tracking of slow moving underwater creatures [1], [2], [5]. Also, in the micro and nano-scale, for medical and biological use for internal screening procedures and treatment delivery [3], [6], [9].

### **1.4 PROBLEM STATEMENT**

Existing propulsion mechanisms for precision maneuvering and inspection AUVs are mechanically complex and costly in their design and construction and often cannot

produce continuous thrust. Consequently, there is need for a suitable propulsion system that can provide continuous thrust and is simpler and more cost effective to build.

## **1.5 CONTRIBUTIONS**

Aside from the several fluid dynamics principles that this work is based upon and the cited works of other researchers, all the design, fabrication, testing and evaluation of experimental data involved in this thesis is done by the author. This research focuses on the design and evaluation of a new, simple and low cost propulsion system prototype suitable for low-speed maneuvering underwater vehicles. The propulsion system proposed here consists primarily of a syringe and a plunger driven by a linear actuator and uses different intake and outflow nozzles to provide continuous propulsive force.

Additionally, in comparison to other functionally similar propulsion mechanisms (e.g. synthetic vortex-ring jet thrusters [2], [6], [11]), the proposed propulsion system deals with the issues relating to the loss in forward thrust caused by the inflow of fluid through the orifice of these thrusters. Also, this work provides some insight into the areas of consideration and the challenges involved with research on underwater vehicles and systems that is useful for further work on AUVs at the University of Denver Unmanned Systems Research Institute (DU<sup>2</sup>SRI).

## **1.6 THESIS ORGANIZATION**

The organization of this thesis is as follows. Chapter 2 provides a literature review where background information on research related to various underwater vehicles, applications and propulsion schemes are discussed. Chapter 3 describes the proposed syringe-plunger propulsion mechanism, the initial direct thrust measurement experiments performed and the results obtained. Chapter 4 discusses the kinematics and dynamics

theory of the test vehicle used to further evaluate the propulsion system and Chapter 5 details the test vehicle apparatus as a Mechatronic system. Chapter 6 presents the experimental and simulation results obtained with the test vehicle. Finally, Chapter 7 provides conclusions and recommendations for future work.

## **CHAPTER 2: LITERATURE REVIEW**

In the following a summary of research on various underwater vehicles and their propulsion mechanisms including: conventional propeller-driven AUVs, biomimetic AUVs and precision maneuvering and inspection AUVs is presented.

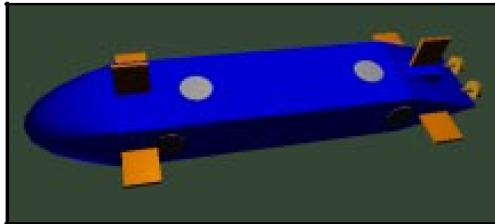
### **2.1 CONVENTIONAL PROPELLER-DRIVEN AUVs**

#### **2.1.1 PHOENIX AUV - NPS**

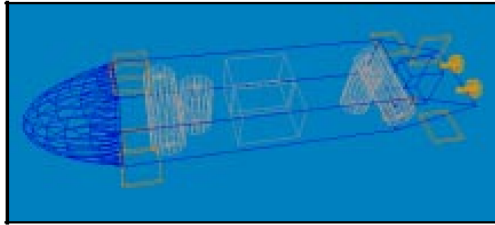
The Naval Postgraduate School (NPS) Phoenix autonomous underwater vehicle (Figure. 2.1), retired, is an AUV for student research in shallow-water sensing and control, its main driving application being shallow-water minefield mapping. The Phoenix is made of aluminum, water tight to 8m depth, neutrally buoyant at about 176-198 kg and has a hull length of 2.2m (Table 2.1). Physical control of the Phoenix is done by means of multiple propellers, thrusters, plane surfaces and sonars [12], [13]. Among its various applications are artificial intelligence (AI) implementations for multisensory underwater navigation and a three-layer software architecture for autonomous dynamic control [14], [15].

The three-layer control architecture used is the Rational Behavior Model (RBM) that consists of the strategic level (top layer) responsible for determining long-term mission goals and logic sequencing, the tactical level (middle layer) in charge of system monitoring and sensor analysis to determine vehicle behavior and issuing of control commands to the execution level (lower layer). The execution level is responsible for

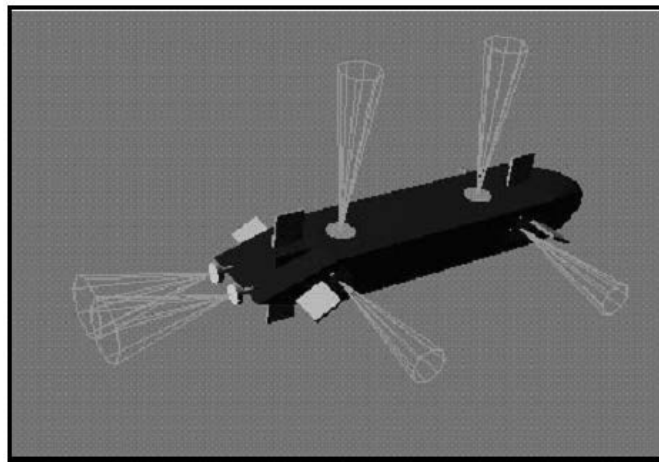
hardware interfacing and reactive real-time physical control [13], [14], [16]. In addition, there is a helper robot software layer whose role is to assist human operators with mission details specification and autonomous high-level source code generation [16]. Virtual world simulations and in-water testing of an auto-generated mission are used to validate the results for synchronized operation of the RBM onboard the Phoenix [13], [15], [17].



Exterior view of NPS *Phoenix* AUV.



Internal view of NPS *Phoenix* AUV.



Hydrodynamics and Control Visualization of NPS *Phoenix* AUV

*Figure. 2.1: NPS Phoenix AUV [12]*



Weight:	176 -198kg (387-436 lbs)
Hull length:	2.2 m (7.2 ft)
Design depth:	6.1 m (20 ft)
Endurance:	90 – 120 mins at 1m/s (2 knots)
Propulsion:	Twin bidirectional propellers, 2 cross-body in-line bidirectional propeller thrusters
Thrust force:	22.5N (5 lbs) and 8.9N (2lbs) respectively
Control surfaces:	4 paired plane surfaces (8 fins total)
Standard sensors:	2 forward-looking sonar transducers
	1 downward-looking sonar altimeter
	Water speed flow meter
	Depth pressure cell
	5 rotational gyros

*Table 2.1: Phoenix AUV specifications [12], [13]*

The underwater water environment is quite inaccessible and precarious and so makes monitoring, communication and testing of underwater vehicles and systems extremely complicated. The physical dynamics of rigid bodies underwater and modes of sensor operation are contradictory. Therefore simulation of underwater vehicles in an underwater virtual world is an important advantage that enables rapid design development and real-time real-world comprehensive modelling of all required features and functions. This 3D simulation environment allows for realistic laboratory assessment and experimentation with AUVs as well as repeated testing of all aspects of their control, stability, sensing, autonomy and reliability [12], [15], [17].

### **2.1.2 THE REMUS 100 AUV**

The Remote Environmental Monitoring Units (REMUS) class of AUVs is the product of over 15 years of innovative research and development by Woods Hole Oceanographic Institute and currently the spin-off company, Hydroid LLC. The REMUS 100 (Figure. 2.2) is one of the latest and most widely used REMUS AUV systems. It is

light in weight and designed for operation underwater for up to 100m deep. The REMUS 100 AUV is 160cm long, 19cm in diameter and weighs about 38.5kg in air [18], [19].



*Figure. 2.2: REMUS 100 AUV [19]*

Its various applications include: hydrographic surveys, mine countermeasure operations, harbor security operations, environmental monitoring, debris field mapping, search and salvage operations and scientific sampling and mapping. The REMUS can be easily transported and stationed by a two-man team. REMUS 100 is the instrument of choice for shallow-water mine counter measure operations for the United States Navy due to its compact size and weight, ease of operations, proven reliability, power and versatility [18], [19].

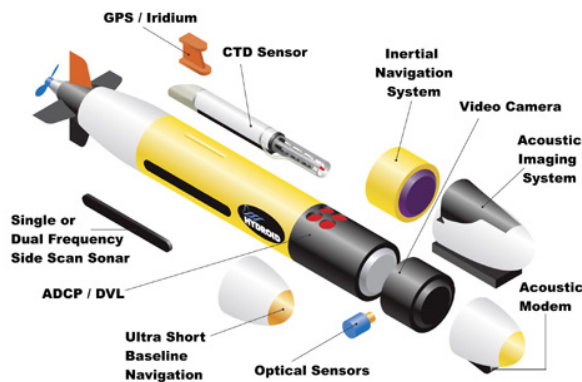


*Figure. 2.3: REMUS 100 AUV standard configuration and sensors [18]*

Although a stock REMUS 100 is equipped with a broad range of standard sensors (Table. 2.2, Figure. 2.3), it can be configured to include a vast array of customer specified

sensors and payloads to meet unique mission requirements. Over the years, various research scientists, engineers and students have developed numerous additional sensor packages and payloads that can be interfaced to the REMUS 100 AUV.

Vehicle diameter:	19 cm (7.5 in)
Vehicle length:	160 cm (63 in)
Weight in air:	38.5 kg (85 lbs)
Trim weight:	1 kg (2.2 lbs)
Maximum operating depth:	100 m (328 ft)
Endurance:	22 hrs at 1.5 m/s (3 knots) >8 hrs at 2.6 m/s (5 knots)
Propulsion:	Direct drive DC brushless motor to open 3-bladed propeller.
Control surfaces:	2 coupled yaw and pitch fins
Navigation:	Long baseline Ultra short baseline (USBL) Doppler-assisted dead reckoning Inertial navigation system GPS
Transponders:	4 transponders: 20 – 30 kHz operating frequency range.
Tracking:	Emergency transponder Mission abort In-mission tracking
Software:	VIP-based laptop interface for programming, training, post-mission analysis, documentation, maintenance, and troubleshooting.
Data exporting and reporting:	HTML report generator and ASCII text export

*Table 2.2: REMUS 100 AUV specifications [18], [19]*

Research conducted at the NPS Center for Autonomous Vehicle Research (CAVR) relating to the obstacle avoidance autonomy issues of the REMUS 100 AUV shows that the REMUS’ normal altitude control “auto-pilot” is unable to sustain a safe elevation over sharp rises in the ocean floor of 45 degrees or greater using only the RDI

Doppler Velocity Log [19], [20]. To solve this problem a new primary obstacle avoidance sensor, the ProViewer 450-15 multi-beam sonar, is installed to enable easy target detection and tracking and optimal obstacle path planning in dynamic conditions. It is mounted vertically and forward facing on the REMUS [21].

Further research proves the spline addition method to be an optimal path planner as it provides robust and reactive obstacle avoidance while optimizing the vehicle's information gathering sensors and allowing for a look-ahead pitch controller. These make up a responsive “back-seat driver” for the REMUS' normal altitude control “auto-pilot” that improve its endurance in unknown environments [19].

The REMUS 100 AUV is also in use by the Heriot-Watt University's Ocean Systems Laboratory (OSL), Scotland, as a simulation platform for a variety of research work regarding autonomous underwater vehicles. For example in [22], based on observed simulation and experimental data from the REMUS 100 AUV, experiments show how an adaptive planner system for autonomous mission diagnosis and repair is able to do maintenance and keep an AUV running during missions. This planner enables the AUV to appropriately and efficiently adapt mission plans to gaps in an operation. Also in [23], the REMUS 100 is used to demonstrate the use of a logic-based scheme for hierarchical distributed representation of knowledge in autonomous underwater systems. Knowledge exchange is initiated between the status monitoring and the adaptive mission planner embedded agents and it is shown that both sub-systems can interchange information and remain domain independent during their communication with the AUV platform while performing a mission.

## 2.2 BIOMIMETIC AUVs

Biomimetic Autonomous Underwater Vehicles (BAUVs) are biologically-inspired autonomous underwater vehicles typically designed to mimic the propulsive capabilities and swimming mechanisms of fish and other underwater creatures. The biological study of underwater creatures offers inspiration for BAUV designs achieving energy efficiency, stealth and maneuverability [3]. In this regard, the functionality of the biological source of inspiration is imitated by way of robot/vehicle designs relying on standard mechanical principles assembled in a somewhat unconventional manner. In recent years, research interest in “artificial fish” is growing significantly due to the attractive promise of being able to take advantage of optimizations attained over millions of years [4], [24].

In [6], a BAUV is presented which imitates the ability of cephalopods to travel underwater by means of pulsed jet propulsion. It has been proven that more propulsive force is produced due to ejection of a discontinuous stream of fluid and the resulting creation of vortex rings at the nozzle exit plane compared to that generated by just a continuous jet [10], [25]. Serchi et al. [6] design a biomimetic model prototype of the structural and functional features of the *Octopus Vulgaris*. The form of this BAUV is obtained by moulding a silicone cast of an actual octopus thereby resulting in a realistic model of both the exterior and interior of an octopus mantle chamber. The prototype robot is 160 mm long, 95 mm wide, 80 mm tall at the largest cross section and has a total weight of 333.5 g, 212.0 g of which are silicone. The activation cycle (Figure. 2.4) is

based on a cable-driven contraction/release of the elastic mantle chamber. Ejection of fluid through a siphon-like nozzle provides suitable propulsive force for the robot.

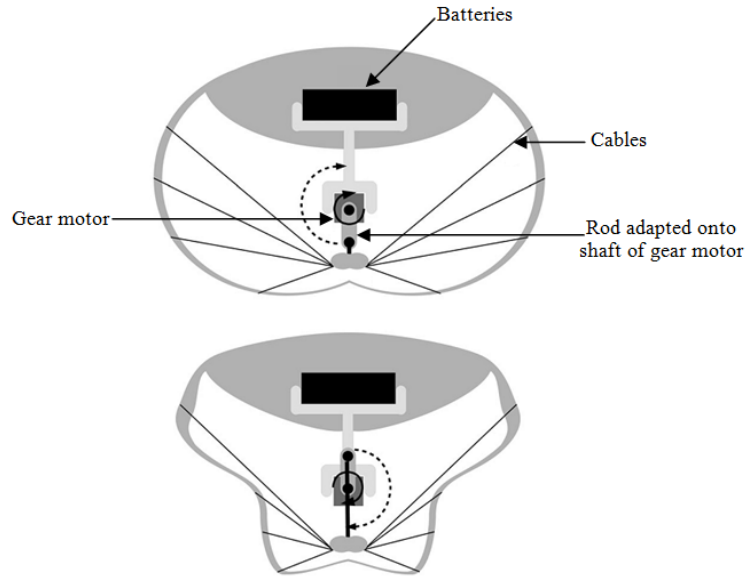
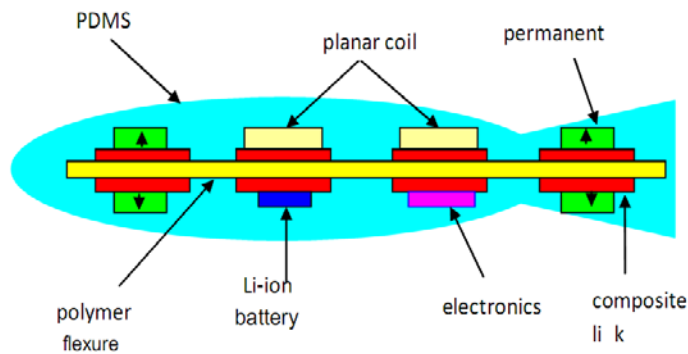


*Figure. 2.4: An illustration of actuator components and activation sequence [6]  
Top: Cross-sectional view of the mantle chamber at the initial stage of the actuation sequence: the external silicone walls are undeformed and the rod is angled  $-90^\circ$ . Bottom: Same cross-section during maximum tension on the cables; the rod is angled  $90^\circ$  and the external silicone walls are folded inward.*

An inverse relationship is found [6] between frequency of pulsation and the average speed of the robot in that, fast pulsation causes inflation of the mantle to become less effective at refilling the mantle cavity with fluid thereby resulting in reduced thrust generation. Their experiments also show that when pulsing at a frequency of 1.5 pps, the soft robot expels water at a maximum jet velocity of 53 cm/s and moves at a maximum speed of 4 cm/s, compared to 1.26m/s jet velocity and 18cm/s maximum travel speed of actual octopuses pulsing at a frequency of 1.67pps. The main limiting factor presented is the passive inflation of the mantle chamber during the refill phase which introduces inefficiency due to the loss in forward thrust caused by inflow of fluid through the nozzle.

E. Lee [26] presents the design of a flexible, biomimetic, micro-robotic fish that leverages the energy saving characteristic of fish. The body of the fish is made of soft material and embedded with electromagnets (Figure. 2.5). Triggering the electromagnets that correspond to particular muscle groups propagates patterns of muscle activity. The biomimetic fish has piezoelectric polymer sensors on its body surface to measure the local fluid flow pressure. It automatically turns off the muscle actuators when it senses vortices in the surrounding fluid so that its body wave can be passively produced by interaction with the oncoming flow of water. The robot fish saves energy firstly by operating at its natural frequency to minimize energy consumption and also by storing the power generated for positive work as elastic energy and then utilizing it later for negative work. Further, the electromagnets of the fish can enable reconfiguration to accomplish certain collaborative tasks by physically connecting with others.



Schematic design of microrobotic fish ( top view ). It has four rigid links connected by a compliant flexure. Planar coils and permanent magnets actuate the fish. Li-ion battery and electronics are located on the opposite side of the planar coils. The entire system is encapsulated by PDMS polymer.

*Figure. 2.5: Schematic of a soft biomimetic micro-robotic fish [26]*

X. Deng and S. Avadhanula [7] discuss the design, fabrication, and force measurement of a centimeter scale micro-underwater vehicle that is an artificial replica of a boxfish. In spite of the fact that such tiny underwater microrobots have limited payload

capacity and slower swimming speed, they are cost-effective in their fabrication and deployment, highly maneuverable and very attractive for missions in underwater environments which are inaccessible by larger size underwater microrobots. In particular recent research has found that a major reason for the hydrodynamic stability of boxfish is there boxy shape. It enables them to efficiently keep to their swimming trajectory and near zero turning radius even in turbulent waters by changing the flow of water around them thereby setting up counter-rotating vortices which in effect act as self-correcting forces [27].

In [7] a micro-robotic fish with a rigid body propelled by an oscillating tail fin and steered by a pair of independent side fins developed (Figure. 2.6). The prototype boxfish has a body length of 12mm with a 10mm long tail fin and weighs 1 gram. PZT actuators independently control and amplify the oscillation of the fins by driving four-bar mechanisms. It is observed that with a 150V peak-to-peak sinusoidal voltage input with a frequency of 6Hz, the forces generated by the tail fin are quite large with amplitude almost equal to the weight of the fish, but the mean force is only about 10% of the robots' weight.

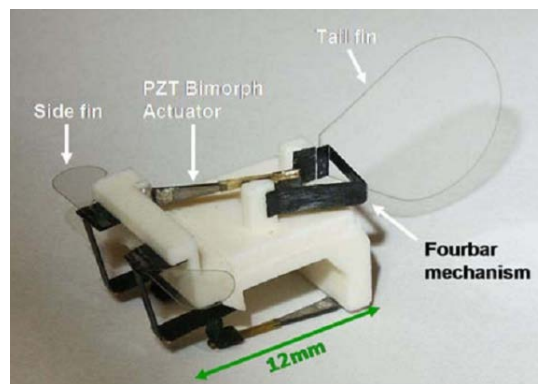


*Figure. 2.6: The boxfish prototype [7]*



## 2.3 PROPULSION SYSTEMS FOR SMALL, COMPACT, LOW-SPEED MANEUVERING AUVs

### 2.3.1 SYNTHETIC VORTEX-RING JET THRUSTERS

The idea behind this propulsion scheme stems from the pulsed jet propulsion method used by sea creatures such as salp, squid and jellyfish, which propel themselves by pulsing water out of a cavity in their body. The concept of these thrusters is similar to that presented in [6] but their physical construction and actuation methods are different. These jet thrusters consist of a cylindrical chamber with a synthetic vibrating membrane at one end and an orifice at the other. Water is drawn into the chamber from around the orifice during the membrane's downstroke and ejected through the same orifice during the upstroke, creating a vortex ring [2], [11], [28]. A sequence of vortex rings results from periodic vibration of the membrane, creating a jet-like structure (Figure. 2.7). A propulsive force is generated as a result of transferral of net momentum to the fluid due to the vortex rings fluid structure.

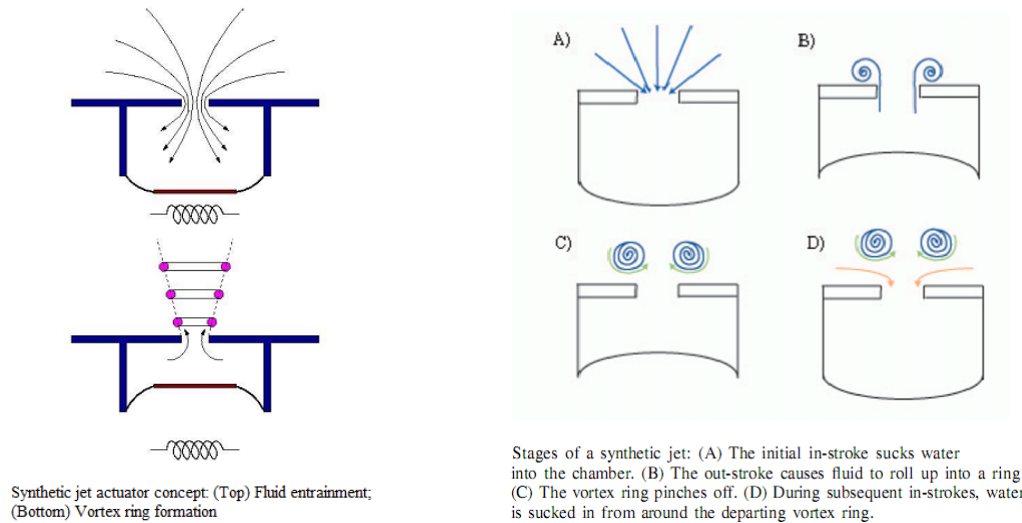


Figure. 2.7: An illustration of synthetic jet actuator operation [2], [11]

Synthetic jet thruster prototypes have been designed and built to study the flow patterns created and measure the forces produced by the jets [2], [11], [29]. The main parts of the mechanism are: an orifice plate, a fluid chamber, a flexible membrane and an actuator. The membrane is a thin rubber sheet and is attached to the actuator via a metal disk glued to the membrane's underside. Different actuators can be used with these jet thrusters including solenoid valves and voice coil actuators. In [2] voice coil actuators are used that allow a large degree of control in driving the membrane.

For a fixed mechanical implementation with an automated experimental apparatus, average thrust force measurements and a genetic algorithm are used to find an optimal set of actuator parameters such as the frequency, amplitude and velocity profile of the membrane's movement [2]. It is found that the maximum propulsive force that can be produced by the synthetic jet is approximately 0.25N using maximum power. Also, it is found that thrust increases proportionally with frequency and that the optimal waveform to send to the synthetic jet thruster is one that causes the membrane to pull fluid in quickly and push it out slowly [2]. The sucking effect is predicted to cause a drop in the overall thrust produced by these thrusters but the magnitude of this reduction is difficult to model or quantify [2], [11].

Overall, these actuators are desirable in many ways: they are relatively simple and compact mechanical structures, they can be installed in small AUVs in such a way that there are no appendages protruding into the surrounding flow and have been shown to be a valid approach for underwater vehicles for tracking slow moving sea creatures that swim at speeds between 2 and 10 cm/s. However they have several downsides as well,

including: that they are fairly inefficient since the loss in forward thrust force caused by the inflow of fluid through the orifice is difficult to predict and they provide forces primarily in one direction and hence are usually paired.

### 2.3.2 THE COANDA JET DEVICE

The coanda effect is the tendency of a high pressure fluid jet to be attracted to and attach itself to a nearby curved surface. When a nearby wall does not allow the surrounding fluid (essentially the same substance) to be entrained towards the jet, the jet moves towards the wall instead. This effect is mainly used for air jet control applications such as increase of the aerodynamic lift of aircrafts and increase of the throw of ceiling mounted diffusers in air conditioning, but is also applied to water such as in oscillatory flow meters, automobile windshield washers and for debris separation in hydropower screens.

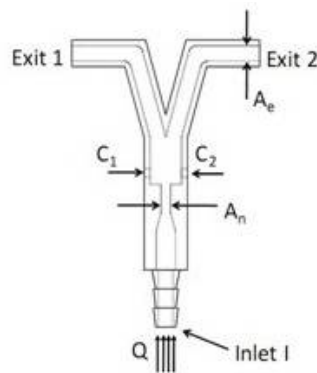


*Figure. 2.8: An Illustration of the basic coanda jet device shape and geometry [1]*

For the Coanda Jet Device (CJD) (Figure. 2.8), a high pressure water jet is supplied through a nozzle inlet and depending on which of the two control ports  $C_1$ ,  $C_2$  is open, the water jet attaches itself to either wall and then exits through either exit [1], [5], [9]. The Coanda effect is utilized at the control ports to switch the direction of the water

jet between the available exits. A prototype CJD is fabricated for static force performance evaluation using a TCS M400K micropump and an MLP 10N load cell and the average force measured to be 0.125N.

Two other experiments are also performed [1], [5] to evaluate the dynamic force performance and speed response of the CJD in comparison to a conventional propeller-type thruster, with a solenoid actuator used to operate the control ports of the CJD. The CJD and propeller-type thruster are activated, allowed to reach steady state, then a change of direction is commanded for “direct” and “indirect” force measurement setups. Despite the introduction of reaction effects due to the spring-back of the solenoid valve’s return spring, it is observed that the CJD provided comparable rise time, improved settling time and reduced reaction forces when compared to a conventional propeller-type thruster [1], [5].

Further, a prototype test vehicle (Figure. 2.9) with a nested structure CJD actuator system (for 2 DOF motion) is fabricated and tested [1] while operating the vehicle in a tethered setup. Two different sets of experiments are carried out to characterize the forward motion and maneuvering characteristics of the test vehicle respectively. The vehicle achieves a steady-state forward velocity of approximately 0.13m/s and a yaw rate of approximately 1rad/s [1]. Also in [5] a full 4DOF vehicle design (Figure. 2.10), with the CJD device miniaturized and incorporated into it, is constructed and presented with some preliminary performance metrics.

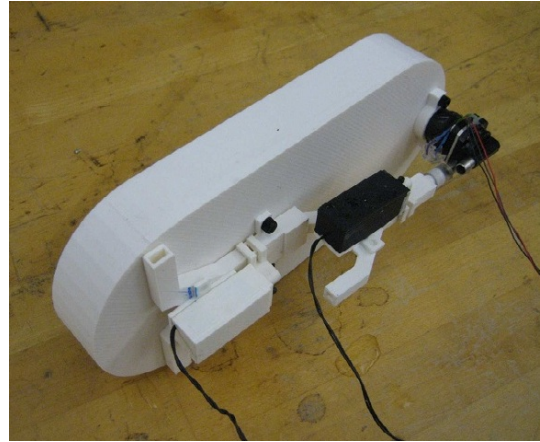
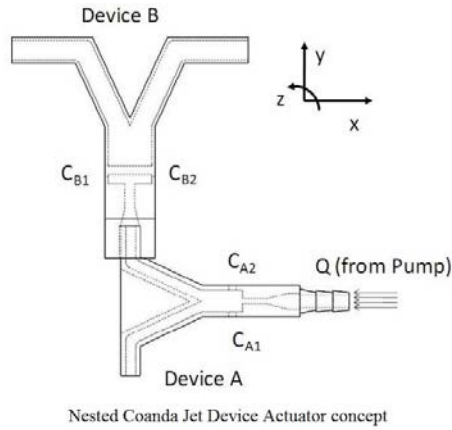
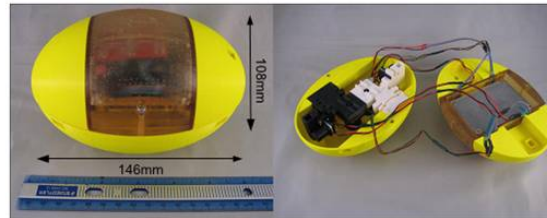


*Figure. 2.9: Nested coanda jet device actuator and first generation prototype test vehicle [1]*



Photographs of the prototype robot and its internal components.

TABLE OF ROBOT PARAMETERS

Mass	$\sim 900g$
Forward Speed	$\sim 0.4m/s$
Turning Rate	$\sim 150^\circ/s$

*Figure. 2.10: Second generation prototype AUV: CJD system imbedded into the hull of the vehicle [5]*

The performance of the test vehicle presented in [1], [5], [9] with the nested CJD mechanism used for propulsion and maneuvering is quite compelling for low-speed precise maneuverability using high-speed switching of water jets. Also, the CJD system imposes minimal reaction forces and moments when reversing flow and can be wholly encapsulated in a compact, smooth, streamlined hull while still allowing the pumps and valves to access the ambient fluid [1], [5], [9]. Still, this mechanism has a number of

limitations including mechanical complexity in construction and the inability to provide bidirectional thrust for every degree of freedom.

In conclusion, having gone over the modes of operation and applications of various types of AUVs in use and under research to-date, the proposed syringe-plunger propulsion system presented in this thesis offers many advantages, particularly for the small, compact, slow moving precision AUVs in comparison to the propulsion mechanisms presented above for the same.

## CHAPTER 3: THE SYRINGE-PLUNGER PROPULSION MECHANISM

### 3.1 OVERVIEW

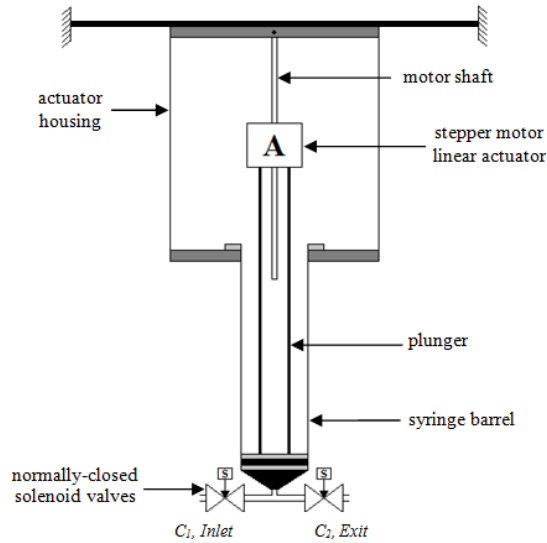


*Figure 3.1: Schematic illustration of the proposed syringe-plunger propulsion system*

The propulsion mechanism proposed in this work (Figure 3.1) consists of a syringe and a plunger attached to a linear stepper motor actuator. The linear actuator is used to move the syringe plunger up and down inside the syringe barrel, thereby drawing in and pushing out fluid (water) through the syringe orifice. Solenoid valves are used to create different intake and outflow orifices and to manage the flow of water at each orifice.

Linear actuators are actuators that create motion in a straight line. Electro-mechanical linear actuators, such as stepper motors, operate by converting the rotary

motion of an electric motor to linear displacement through a threaded shaft. The electric motor is mechanically connected to rotate a lead screw.

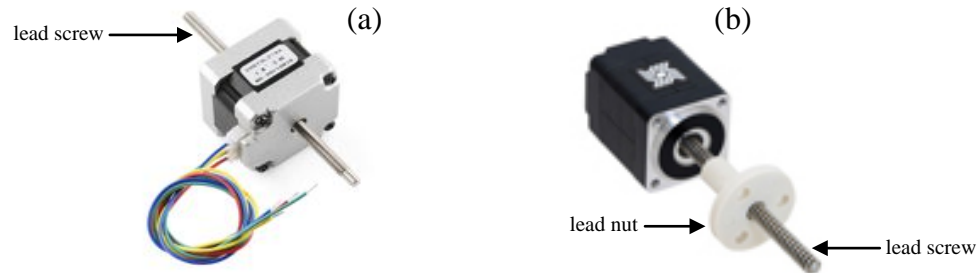


*Figure 3.2: (a) Travelling-screw linear actuator; (b) Travelling-nut linear actuator*

A travelling-screw linear actuator (Figure 3.2.a) has the lead screw passing entirely through the motor. Restraining the lead screw from spinning causes the motor to move up and down the lead screw. This type is used for the direct thrust measurement experiments, described in Section 3.2, as it facilitates placement of the force sensors used to determine the resultant force output of the propulsion system. On the other hand, a travelling-nut linear actuator (Figure 3.2.b) has the motor permanently attached to one end of the lead screw. As the motor spins the lead screw, restraining the lead nut from spinning causes it to travel up and down the lead screw. This type is used for the test vehicle experiments, described on Chapter 5, as it enables installation of the propulsion mechanism in the vehicle, while allowing for attachment of the other components necessary for the experiment.

Connecting a linkage, i.e. a load (the plunger in this case), to the motor and lead nut respectively converts the rotary motion of the lead screw to usable linear displacement. Stepper motor linear actuators are relatively cheap and used mostly for applications that require repeatability, automation, fine resolution and high accuracy.



They are chosen for use in this work primarily for this reason, to facilitate determination of the speed and displacement of the plunger in the syringe barrel.

The efficacy of the proposed propulsion system design was assessed via two phases of experiments:

1. Direct thrust measurement experiments to determine the net propulsive force output of the mechanism.
2. Experiments with the mechanism installed in a test vehicle to evaluate and model the resultant propulsive force produced and estimate the speed performance characteristics achievable by a vehicle employing the propulsion system.

### **3.2 DIRECT THRUST MEASUREMENT EXPERIMENTS**

These experiments are performed to determine the net propulsive force of the syringe-plunger mechanism for two different experimental setups. They are performed for various actuation sequences where the speed of the plunger movement in the syringe is varied for a fixed mechanical implementation, i.e. fixed syringe orifice, syringe barrel size, plunger diameter, water control volume and solenoid valve geometry. The plunger is rigidly attached to the motor and therefore is pulled up and pushed down the syringe barrel when the motor moves during the upstroke and downstroke actions respectively.

For these direct thrust experiments the linear stepper motor is controlled using the X MOS microcontroller and a stepper motor driver. Square wave signal commands of 50% duty cycle are sent from the X MOS microcontroller, via the motor driver, to the motor to control its direction of movement, linear displacement and speed. A LabView

software program and the NI DAQ device are used to obtain voltage measurements from the load cell when force is applied to it.

### 3.2.1 EXPERIMENTAL SETUP 1

Figure 3.3 shows a schematic of the first experimental setup (Figure 3.4) of the syringe-plunger mechanism, set up to draw and push out water from the same orifice during the plunger upstroke and downstroke respectively. This setup only produces net thrust in one direction. These experiments are performed to determine the net propulsive force of the syringe-plunger mechanism and also to compare the results with those of the synthetic jet thruster systems [2], [11] where a synthetic vibrating membrane is used to draw and push out water into and out of a cylindrical chamber through a single orifice.

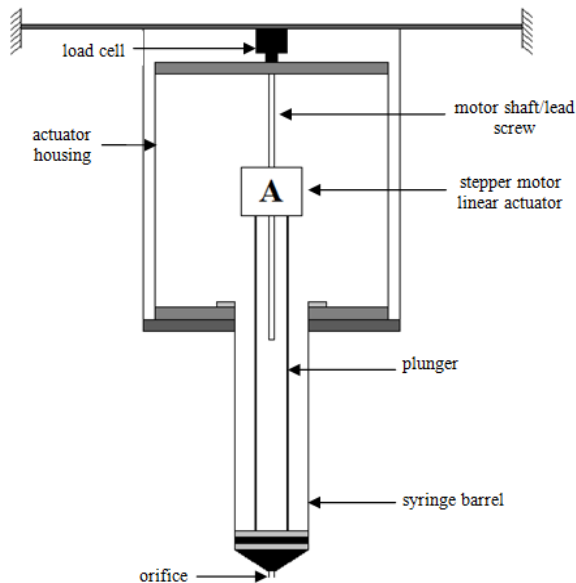


*Figure 3.3: Schematic illustration of experimental setup 1*

The apparatus used for these experiments comprises of the following hardware and software components:

- ❖ A travelling-screw linear stepper motor actuator (NEMA 17, 0.4A Bipolar, 12V)

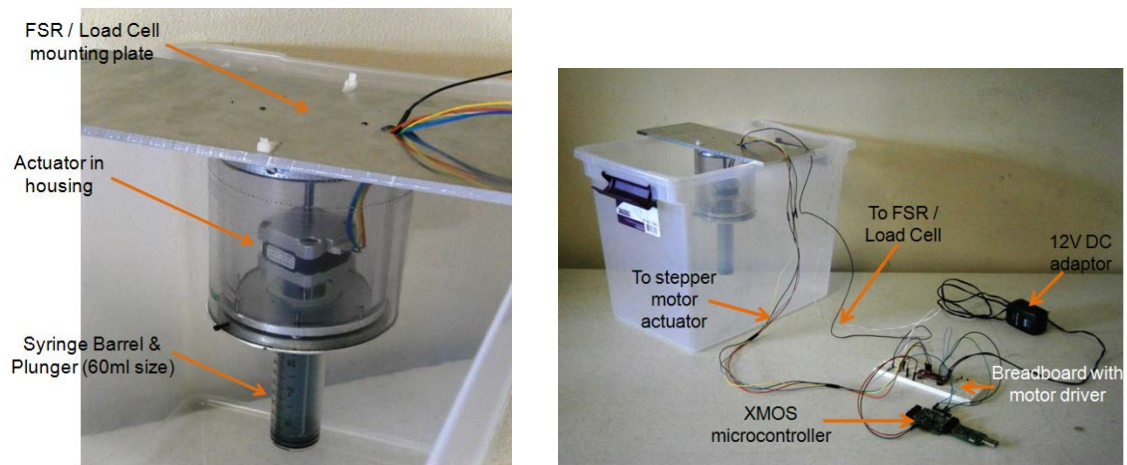


*Figure 3.4: An illustration of experimental setup 1*

- ❖ Stepper motor driver (Sparkfun EasyDriver stepper motor driver)
- ❖ Syringe barrel and Plunger (60ml size)
- ❖ XMOS XK-1A microcontroller and xTIMEcomposer Studio Development Environment/Software
- ❖ Force Sensitive Resistor, FSR (0.5" diameter, sensing area)
- ❖ Flexiforce Pressure, FFP Sensor, (piezoresistive FSR sensor, 0-25lbs sensing range)
- ❖ A force sensing load cell (FC22 Compression Load Cell, 0-10 lbf/0-44.48N force range)
- ❖ 12V and 5V DC power adaptors
- ❖ A Data Acquisition (DAQ) device (model: NI DAQ USB-6008)
- ❖ LabView software
- ❖ 2 Normally-closed Solenoid valves, 12V 6W
- ❖ 2 Single-side stable TTL (Transistor–transistor logic) relays, TF2-5V

The actuator housing and sensor attachment plate are fabricated from clear plastic, impact-resistant polycarbonate round tubes of different wall thicknesses and different inner and outer diameter sizes and an unpolished (mill) finish multipurpose aluminum (Alloy 6061), 1/4" thick, 12"x12" bar.



*Figure 3.5: An illustration of the actuator housing parts*

Three force sensors (Figure 3.6) are evaluated for tests with this initial setup. These include: the Force Sensitive Resistor (FSR) sensor, the Flexiforce Pressure (FFP) sensor and the force sensing compression load cell. FFP sensors have greater accuracy than FSR sensors of about  $\pm 3\%$  while the force sensing load cell has superior accuracy and higher reliability than both the FFP and FSR sensors. The results presented in Section 3.3 of this chapter are obtained using the FC22 force sensing compression load cell.



*Figure 3.6: From left to right: The FSR sensor; The FFP sensor; The FC22 Load cell*

The load cell has a ratiometric voltage output span of up to 5V and is first calibrated to obtain an equation describing the relationship between the voltage output in Volts and the applied force in Newtons. This is done by measuring and recording the voltage outputs from the load cell when known force values/weights are applied to it and then plotting the Force (N) vs. Voltage Output (V) data. Next, the curve fitting function in MATLAB is used to find the equation relating the Voltage Output (V) to Force (N). This equation (Equation 3.1) is used to determine the force measurements from the voltage readings obtained from the load cell during experiments.

$$F (N) = 4.4036V - 0.00137 \quad (3.1)$$

### 3.2.2 EXPERIMENTAL SETUP 2

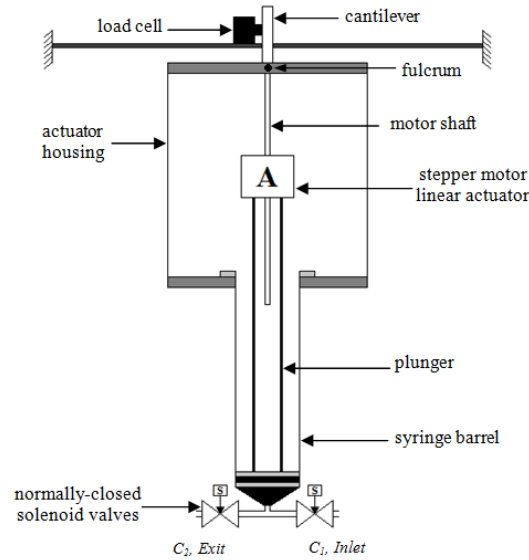


*Figure 3.7: Schematic illustration of experimental setup 2*

Figure 3.7 provides an illustration of the second direct force experimental setup, set up to draw and push out water from two different orifices consecutively during the plunger upstroke and downstroke.

In this second setup, two solenoid valves are attached to the end of the syringe to create different intake and outflow orifices. The control ports  $C_1$  and  $C_2$  are used to manage the flow of water at the inlet and exit orifices. The control ports  $C_1$  and  $C_2$  are operated by activating two independent normally-closed solenoid valves. During the plunger upstroke, control port  $C_1$  is opened (control port  $C_2$  must remain closed) and water is drawn into the syringe barrel through the inlet orifice. Opening of control port  $C_2$  (with control port  $C_1$  now closed) during the plunger downstroke, allows the fluid to be pushed out through the exit orifice. Off-the-shelf solenoid valves (Figure 3.8) with a response time of 20ms are used. By responding to signal commands from the X MOS microcontroller, two independent single-side stable TTL relays are used to open and close the solenoid valves as required during the experiments.



*Figure 3.8: Left: Normally-closed Solenoid Valve; Right: 5V TTL Relays*

### **3.3 FORCE MODEL**

The force output model of the direct dynamic thrust measurement experiments is produced based on simple fluid mechanics principles and several assumptions outlined below.

#### **ASSUMPTIONS:**

- ❖ Inviscid and incompressible fluid (i.e. constant mass density  $\rho$ ).

- ❖ Minor pipe losses due to elbows and small contractions and expansions at the syringe exit orifice and valve inlet and outlet orifices are neglected.
- ❖ Frictional losses due to plunger movement in the syringe barrel are considered negligible.
- ❖ Reaction effects due to spring back of solenoids are neglected. (Setup 2)

### 3.3.1 EXPERIMENTAL SETUP 1

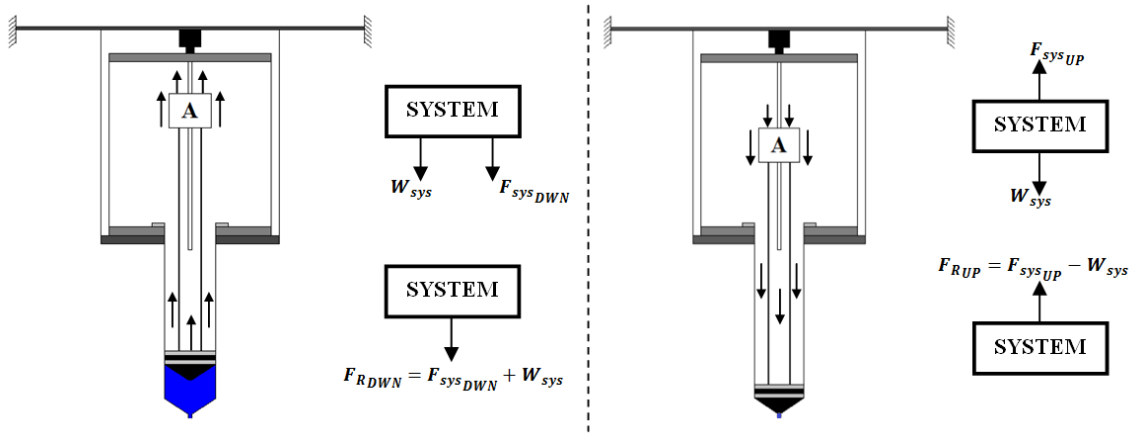


Figure 3.9: Schematic illustration of the free body force diagram for setup 1 thrust measurement experiments.  
(left: Plunger Upstroke; right: Plunger Downstroke)

In general, by use of the continuity equation (Equation 3.2) and the conservation of linear momentum principle (Equation 3.3) for open systems, the theoretical resultant net output force  $F_{NET}$ , of the propulsion mechanism can be found. In addition, for this experimental setup, the line of action of the resultant forces on the system due to the plunger upstroke ( $F_{DWN}$ ) and downstroke ( $F_{UP}$ ) is parallel and coincident to the force due to gravity (Equation 3.4) acting on the system. This is taken into account while calculating the resultant net output force  $F_{NET}$ , of the mechanism as shown in the free body force for this experimental setup (Figure 3.9) and Equation 3.5.

This ensures complete modelling of the resultant net output force  $F_{NET}$ , of the syringe-plunger propulsion mechanism in comparison to synthetic jet propulsion systems [2], [11] where only the force produced during the out-stroke motion of the synthetic membrane is modelled and the obvious reduction of thrust due to the suction effect of the membrane upstroke is neglected.

$$\left. \begin{aligned} \dot{m} &= constant \\ \dot{m}_{inlet} &= \dot{m}_{exit} \end{aligned} \right\} \quad (3.2)$$

$$\dot{m}(V_{exit} - V_{inlet}) = \sum F \quad (3.3)$$

$$F_G = W_{sys} = mg \quad (3.4)$$

$$F_{T,1} = F_{NET,1} = |F_{UP}| - |F_{DWN}| \quad (3.5)$$

where:

$F_{UP} = F_{R_{UP}}$  = resultant thrust force on the system due to plunger downstroke

$F_{DWN} = F_{R_{DWN}}$  = resultant thrust force on the system due to plunger upstroke

$F_T$  = resultant net thrust force on the system

$\dot{m}$  = mass flow rate

$V$  = fluid velocity

$F$  = resultant force

$F_G$  = force due to gravity

$g$  = acceleration due to gravity

### 3.3.2 EXPERIMENTAL SETUP 2

For the experiments with the second setup (Figure 3.10), the line of action of the resultant forces on the system due to the plunger upstroke ( $F_{DWN}$ ) and downstroke ( $F_{UP}$ ) is perpendicular to the force due to gravity acting on the system. Therefore here, the effect



of the gravitational force on these resultant forces on the system is considered negligible. The net thrust output ( $F_{NET,2}$ ) is obtained by combining the  $F_{DOWN}$  and  $F_{UP}$  forces on the system as shown in equation 3.6.

$$F_{T,2} = F_{NET,2} = |F_{UP}| + |F_{DOWN}| \quad (3.6)$$

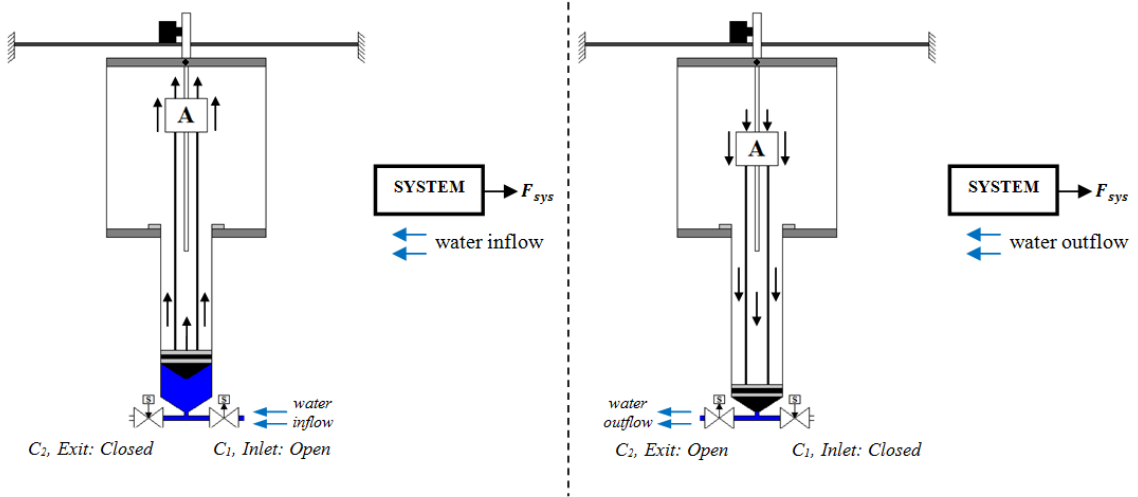


Figure 3.10: Schematic illustration of the free body force diagram for the setup 2 thrust measurement experiments.  
(left: Plunger Upstroke; right: Plunger Downstroke)

### 3.4 EXPERIMENTAL RESULTS AND DISCUSSION

The direct thrust measurement experiments described in Section 3.2 above are performed for various actuation sequences where the linear speed of the plunger movement is varied from 0.25cm/s to 0.893cm/s by changing the frequency of the signals sent from the microcontroller. This is done to determine the influence of the type of flow (as described by the Reynolds number) through the syringe and valve orifices on the thrust output of the mechanism. Specifically, experiments for three different actuation sequences/cases are carried out.

1. **CASE 1:** Equal plunger upstroke and downstroke speed.

2. **CASE 2:** Plunger upstroke speed is faster than the downstroke speed. The upstroke speed is kept constant at 0.781cm/s while the downstroke speed is increased from 0.25cm/s to 0.625cm/s for each consecutive set of experiments.
3. **CASE 3:** Plunger downstroke speed faster than the upstroke speed. The downstroke speed is kept constant at 0.893cm/s while the upstroke speed is increased from 0.25cm/s to 0.781cm/s for each consecutive set of experiments.

The disparity in the maximum upstroke and downstroke plunger speeds for cases 2 and 3 above is due to hardware failures and challenges with the linear actuator during the course of these experiments. For each set of experiments the force measurement data obtained is evaluated using the trapezoidal rule for numerical integration and Equations 3.2 – 3.6 to determine the resultant thrust due to plunger upstrokes and downstrokes and therefore the resultant net thrust output of the propulsion mechanism.

The resultant net thrust output results for each actuation case for both experimental setups and for plunger speeds from 0.25cm/s to 0.893cm/s are presented in Figure 3.11 and Figure 3.12 respectively. The thrust output results for the CASE 3 experiments are normalized for a downstroke plunger velocity of 0.781cm/s. This is done by using Equations 3.2 and 3.3 to determine the difference in the theoretical thrust output for CASE 3 with a downstroke speed of 0.781cm/s instead of 0.893cm/s.

For both experimental setups it is observed that more net thrust output from the propulsion mechanism is generally achieved by actuation sequences that have the plunger upstroke speed being faster than the downstroke speed, i.e. CASE 2. Additionally, for setup 2, for plunger speeds between 0.25cm/s and 0.625cm/s, it is observed that for both

CASES 2 and 3 the greater the difference between the upstroke and downstroke speeds the higher the net thrust produced.

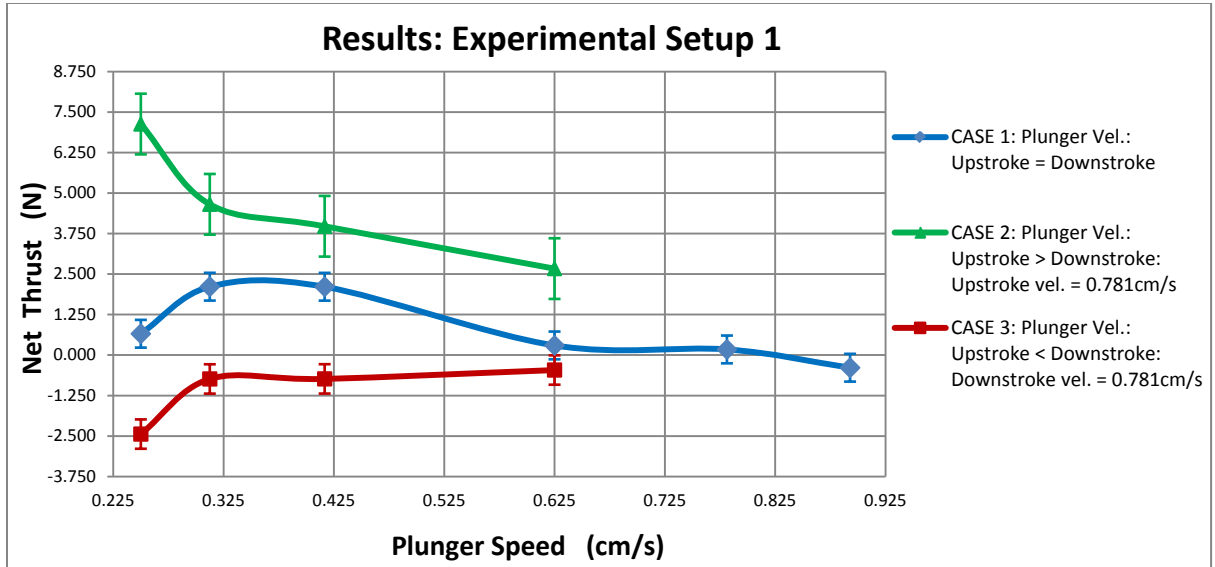


Figure 3.11: Experimental Setup 1: Net Thrust Output Results

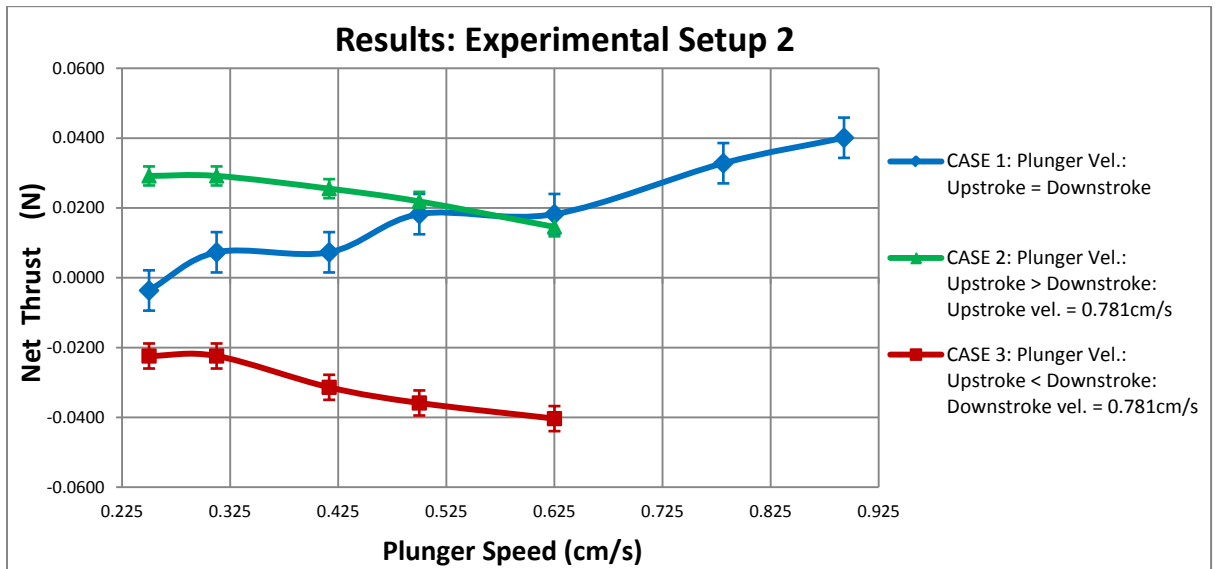


Figure 3.12: Experimental Setup 2: Net Thrust Output Results

The difference in the net thrust output of CASES 2 and 3 is in line with fluid dynamics principles [30], [31] that pressure and energy losses ( $\Delta p$ ) in fluid flow in pipes increase as the velocity of flow ( $U$ ) increases and the flow becomes turbulent (Equations 3.7 and 3.8). For setup 1 in particular, the amount of positive net thrust is mainly due to how much thrust is produced by the downstroke movement of the plunger. The type of flow through the syringe orifice is determined by the Reynolds number (Equation 3.9).

Laminar flow:  $Re < 2300$

Transition flow:  $2300 < Re < 4000$  (3.7)

Turbulent flow:  $4000 < Re$

**and**

Laminar flow:  $\Delta p \propto U$

Transition flow:  $\Delta p \propto U^{>2.0}$  (3.8)

Turbulent flow:  $\Delta p \propto U^{1.7-2.0}$

$$Re = \frac{V_f D}{\nu} \quad (3.9)$$

where:

$V_f$  = fluid velocity;  $D$  = the diameter of the syringe orifice

$\nu$  = fluid kinematic viscosity

The Reynolds number range for the flow of water through the syringe orifice for the plunger velocities between 0.25cm/s to 0.781cm/s is 453.81 to 2836.31, i.e. laminar to transition flow. Higher downstroke plunger speeds cause the flow of water being pushed out of the syringe orifice to be increasingly more turbulent, resulting in higher energy losses in the flow and reduced thrust output.

Further, preliminary investigations are performed to demonstrate that the proposed mechanism can provide enough propulsive force for an arbitrary, small underwater vehicle operating at low speed. The experimental net thrust output results obtained in both setups is compared to the axial drag force  $F_D$  (Equation 3.10) that would act on such a vehicle, with its shape approximated as a smooth sphere. Drag force is the measure of the resistance to motion of a vehicle while it is moving through a fluid and is typically expressed in terms of the drag coefficient,  $C_D$  (Equation 3.11).

$$F_D = \frac{1}{2} C_D \rho A_p V_v^2 \quad (3.10)$$

$$C_D = f(Re, e); \quad Re = \frac{V_v D}{\nu} \quad (3.11)$$

where:

$A_p$  = projected cross-sectional area normal to the direction of the drag force

$e$  = surface roughness

$\rho$  = mass density of fluid

$V_v$  = vehicle velocity

$\frac{1}{2} \rho V_v^2$  = equivalent dynamic pressure

$D$  = the diameter  $D$  of the sphere

$\nu$  = fluid kinematic viscosity

For flow over smooth rigid bodies, the type of flow is considered laminar for Reynolds numbers less than  $10^5$  and turbulent flow Reynolds numbers above  $10^6$  [30]–[32]. At low speeds between 2cm/s and 10cm/s the flow around such a vehicle is laminar with Reynolds number between 4980 and 24900. For this range of Reynolds numbers, the

drag coefficient is (Equation 3.11) 0.45 and the drag force (Equation 3.10) on the vehicle increases from 0.0044N to 0.11N.

Taking the results for CASE 2, setup 1 (Figure 3.11), with plunger speeds of 0.781cm/s and 0.625cm/s for the upstroke and downstroke respectively, the thrust output of the mechanism is 2.6694N. This thrust is much greater than the drag of the spherical vehicle mentioned above for the range of speeds under consideration and hence indicates that the propulsion mechanism can deliver enough thrust to drive such a vehicle. For CASE 2, setup 2 (Figure 3.12), with plunger speeds of 0.781cm/s and 0.625cm/s for the upstroke and downstroke respectively, the thrust output of the mechanism is 0.01458N. This thrust is greater than the drag of the spherical vehicle mentioned above for operating speeds up to approximately 4cm/s and indicates that the propulsion mechanism can deliver enough thrust to drive the vehicle at this speed.

In comparison to synthetic vortex-ring jet thrusters [2] and the coanda jet device [1], it is observed from the results above that setup 1 of the syringe-plunger propulsion mechanism can provide much higher propulsive force than either of them at lower cost and power consumption. The propulsive forces achieved by setup 2 of the syringe-plunger propulsion mechanism are considerably lower. This can be attributed firstly to force measurement error due possibly to the setup design, i.e. symmetry of the placement of the load cell, the cantilever beam and the valve attachments to the syringe. Also, the reduced net thrust output from setup 2 suggests negation of the assumption in Section 3.3 that the pipe losses due to the elbow connections between the syringe exit orifice and the valves are negligible. However the positive results from the evaluation described above

with the arbitrary 0.25m diameter spherical vehicle allow for advancement to the installation of the syringe-valve setup in a proof-of-concept test vehicle for further assessment.

Also, research shows that data in research papers indicates a huge disparity in forces which points to a greater calibration issue with the force sensors in use. Universal calibration and an understanding of the uncertainty analysis involved in force sensing are essential for experimental work and comparison of results across research groups [33], [34].

## **CHAPTER 4: TEST VEHICLE MODELLING**

### **4.1 TEST VEHICLE DESIGN**

A surface vehicle is built at the University of Denver Unmanned Systems Research Institute (DU<sup>2</sup>SRI) to physically test the performance of the syringe-plunger propulsion mechanism prototype, with the solenoid valves used to operate the control ports for production of continuous thrust. The mechanism is installed in the test vehicle and various experiments are performed to evaluate and enable modelling of the resultant force and speed performance characteristics achievable by employing the propulsion mechanism. The experiments are performed for various actuation sequences where the speed of the plunger movement in the syringe is varied for a fixed mechanical implementation, i.e. fixed syringe orifice and barrel size, plunger diameter, water control volume, solenoid valve geometry and vehicle inflow and outflow nozzles.

To ensure ease of modelling and testing, a simple, elliptically shaped, positively buoyant (floating), barge-like design is used. The test vehicle is designed using SolidWorks 3D CAD software and produced using an FDM 3D printing machine. Figure 4.1 provides an illustration of the test vehicle shape and the coordinate system employed for modelling the vehicle's dynamics.



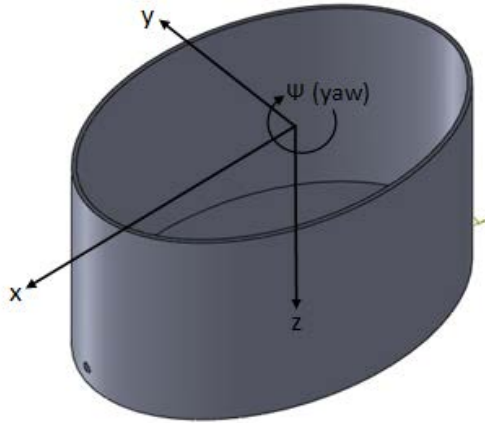


*Figure 4.1: An illustration of the test vehicle shape and coordinate system*

After several design iterations of the test vehicle to ensure optimum installation of the propulsion mechanism in the vehicle while maintaining a smooth outer shape, a final workable design is achieved. An illustration of the test vehicle prototype is provided in Figure 4.2. This first generation test vehicle is designed for one degree of freedom (DOF) movement to simplify the dynamics and control of the vehicle. Hence, the propulsion system is installed in the vehicle such that it provides thrust in the x-direction.

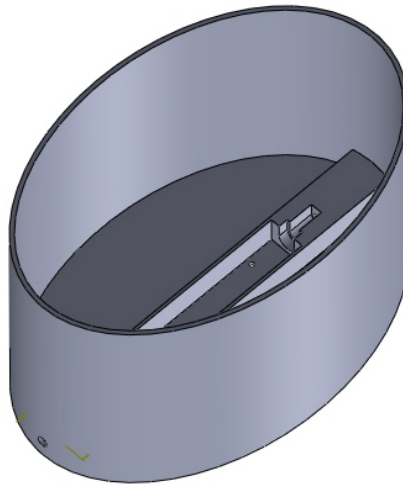


*Figure 4.2: A solid model illustration of the first generation test vehicle*

## 4.2 TEST VEHICLE KINEMATICS AND DYNAMICS

### 4.2.1 ASSUMPTIONS

An accurate model must first be derived to describe the maneuvering and motion control of the vehicle to achieve realistic results. With the movement of the vehicle confined to a maximum of 2DOF (i.e. the 1-2 plane) the following initial assumptions are made to accomplish this:

- ❖ The vehicle behaves as a rigid body.
- ❖ The earth's rotation is negligible as far as acceleration components of the vehicle's center of mass are concerned.
- ❖ The primary external forces that act on the vehicle include propulsion forces  $F_x$  and  $F_y$ , and hydrodynamic forces related to added mass ( $a_{ij}$ ) and pressure drag.

### 4.2.2 EQUATIONS OF MOTION

Rotational and translational Equations of Motion (EOM) are developed by [17], [35], [36] using a Newton-Euler approach and Euler angle transformations. Incorporating weight/buoyancy forces they derive the following EOM for a full six degree of freedom (DOF) model for underwater vehicles:

#### SURGE EQUATION OF MOTION

$$m[\dot{u}_r - v_r r + w_r q - x_G(q^2 + r^2) + y_G(pq - \dot{r}) + z_G(pr + \dot{q})] + (W - B) \sin \theta = X_f$$

#### SWAY EQUATION OF MOTION

$$m[\dot{v}_r + u_r r - w_r p + x_G(pq + \dot{r}) - y_G(p^2 + r^2) + z_G(qr - \dot{p})] - (W - B) \cos \theta \sin \phi = Y_f$$

#### HEAVE EQUATION OF MOTION

$$m[\dot{w}_r - u_r q + v_r p + x_G(pr - \dot{q}) + y_G(qr + \dot{p}) - z_G(p^2 + q^2)] - (W - B) \cos \theta \cos \phi = Z_f$$

### ROLL EQUATION OF MOTION

$$I_x \dot{p} + (I_z - I_y)qr + I_{xy}(pr - \dot{q}) - I_{yz}(q^2 - r^2) - I_{xz}(pq + \dot{r}) + m[y_G(\dot{w}_r - u_r q + v_r p) - z_G(\dot{v}_r + u_r r - wrp - y_{GW} - y_{BB}\cos\theta\cos\phi + z_{GW} - z_{BB}\cos\theta\sin\phi) = Kf$$

### PITCH EQUATION OF MOTION

$$I_y \dot{q} + (I_x - I_z)pr - I_{xy}(qr + \dot{p}) + I_{yz}(pq - \dot{r}) + I_{xz}(p^2 - r^2) - m[x_G(\dot{w}_r - u_r q + v_r p) - z_G(\dot{u}_r - v_r r + wrq + x_{GW} - x_{BB}\cos\theta\cos\phi + z_{GW} - z_{BB}\sin\theta) = Mf$$

### YAW EQUATION OF MOTION

$$I_z \dot{r} + (I_y - I_x)pq - I_{xy}(p^2 - q^2) - I_{yz}(pr + \dot{q}) + I_{xz}(qr - \dot{p}) + m[x_G(\dot{v}_r + u_r r - w_r p) - y_G(\dot{u}_r - v_r r + wrq - x_{GW} - x_{BB}\cos\theta\sin\phi - y_{GW} - y_{BB}\sin\theta) = Nf$$

Equations (4.1) [17], [35], [36]

where:

$W$  = weight

$B$  = buoyancy

$I$  = mass moment of inertia terms

$u_r, v_r, w_r$  = component velocities for a body fixed system with respect to the water

$p, q, r$  = component angular velocities for a body fixed system

$x_B, y_B, z_B$  = position difference between geometric center and center of buoyancy

$x_G, y_G, z_G$  = position difference between geometric center and center of gravity

$X_f, Y_f, Z_f, K_f, M_f, N_f$  = sums of all external forces (body fixed directions)

Also, the three world coordinate frame translation rates are obtained from the body coordinate frame translation rates by use of Equation 4.2.1.

$$\begin{bmatrix} \dot{x} \\ \dot{y} \\ \dot{z} \end{bmatrix} = [R] \begin{bmatrix} u \\ v \\ w \end{bmatrix} \quad (4.2.1)$$

where,  $[R]$  is the body to world rotation matrix [17], [35], [36].  $[R]$  is an orthogonal matrix hence,  $[R]^{-1} = [R]^T$ .

$$[R] = \begin{bmatrix} \cos \theta \cos \psi & \sin \phi \sin \theta \cos \psi - \cos \phi \sin \psi & \cos \phi \sin \theta \cos \psi + \sin \phi \sin \psi \\ \cos \theta \sin \psi & \sin \phi \sin \theta \sin \psi + \cos \phi \cos \psi & \cos \phi \sin \theta \sin \psi - \sin \phi \cos \psi \\ -\sin \theta & \sin \phi \cos \theta & \cos \phi \cos \theta \end{bmatrix} \quad (4.2.2)$$

The three world coordinate frame Euler angle rotation rates are obtained from body coordinate frame rotation rates by use of Equation 4.3.1.

$$\begin{bmatrix} \dot{\phi} \\ \dot{\theta} \\ \dot{\psi} \end{bmatrix} = [T] \begin{bmatrix} p \\ q \\ r \end{bmatrix} \quad (4.3.1)$$

where,  $[T]$  is the body to world translation matrix [17], [35], [36].  $[T]$  is not an orthogonal matrix hence,  $[T]^{-1} \neq [T]^T$ .

$$[T] = \begin{bmatrix} 1 & \sin \phi \tan \theta & \cos \phi \tan \theta \\ 0 & \cos \phi & -\sin \phi \\ 0 & \sin \phi \sec \theta & \cos \phi \sec \theta \end{bmatrix} \quad (4.3.2)$$

### 4.2.3 EXTERNAL FORCES AND MOMENTS ON VEHICLE

#### A. DRAG

Drag force  $F_D$ , represents the resistance encountered by bodies moving through fluids. It explains the need to supply power to keep ground, air, surface and underwater vehicles in motion. As mentioned in Section 3.3, this force is typically expressed in terms of the *drag* coefficient  $C_D$ , defined as,

$$C_D = \frac{F_D}{\frac{1}{2} \rho A_P V^2} = f(Re_L, e) \quad (4.4)$$

$Re_L$  is a dimensionless number that represents the ratio of inertial to viscous fluid forces and helps predict the type of flow around different rigid body shapes moving through fluids . It is given by the equation

$$Re_L = \frac{VL}{\nu} \quad (4.5)$$

where,  $\nu$  represents the fluid kinematic viscosity ( $\text{m}^2/\text{s}$ ). Because of its importance, drag force, specifically the drag coefficient  $C_D$ , and its behavior is well documented in Fluid Dynamics literature for a large number of configurations/rigid bodies shapes and flow conditions, see e.g. [30]–[32].

## B. ADDED MASS AND ADDED MASS COEFFICIENTS

Added mass can be interpreted as a particular volume of fluid particles that are accelerated with a body as it moves through a fluid. The added-mass coefficients for translation generally differ depending on the direction of the body motion. One convenient feature of the added-mass coefficients is their symmetry where,  $a_{ij} = a_{ji}$  [37]. Thus there are twenty-one independent added-mass coefficients and this number is substantially reduced if the body is symmetrical about one or more axes. The test vehicle used in this work is assumed to be top-bottom (x-y plane) and port-starboard (x-z plane) symmetric [35], [36], hence its added mass matrix reduces to (Equation 4.6).

$$M_A = \begin{bmatrix} A_{11} & A_{12} \\ A_{21} & A_{22} \end{bmatrix} = \begin{bmatrix} a_{11} & \cdots & a_{16} \\ \vdots & \ddots & \vdots \\ a_{61} & \cdots & a_{66} \end{bmatrix} = \begin{bmatrix} a_{11} & 0 & 0 & 0 & 0 & 0 \\ 0 & a_{22} & 0 & 0 & 0 & a_{26} \\ 0 & 0 & a_{33} & 0 & a_{35} & 0 \\ 0 & 0 & 0 & a_{44} & 0 & 0 \\ 0 & 0 & a_{53} & 0 & a_{55} & 0 \\ 0 & a_{62} & 0 & 0 & 0 & a_{66} \end{bmatrix} \quad (4.6)$$

where:

$A_{11} = 3 \times 3$  added mass matrix;  $A_{22} = 3 \times 3$  added inertia tensor matrix

$A_{12}$  and  $A_{21} = 3 \times 3$  added static moments matrices

$a_{ij} =$  added-mass coefficients

In many situations especially those involving elongated or cylindrical rigid bodies, three-dimensional added-mass coefficients can be approximated by *strip theory* synthesis, in which the flow at each section can be assumed to be locally two-dimensional [37].

Therefore, for the test vehicle the sum of the external forces and moments [35], [36] are simplified for 2DOF motion and expressed as

$$F_{drag,i} = 1/2 C_{D,i} \rho A_{P,i} V_i^2$$

$$\Sigma X_f = a_{11}\dot{u} - a_{22}vr - a_{62}rr - F_{drag,1} + F_X \quad (4.7)$$

$$\Sigma Y_f = a_{22}\dot{v} + a_{62}\dot{r} + a_{11}ur - F_{drag,2} + F_Y \quad (4.8)$$

$$\Sigma N_f = a_{26}\dot{v} + a_{66}\dot{r} - (a_{11} - a_{22})uv + a_{62}ur + F_Y l \quad (4.9)$$

where:

$i$  = directions 1,2

#### 4.2.4 HORIZONTAL PLANE SIMPLIFICATIONS

For motion in the horizontal (1-2) plane only, the six degrees of freedom EOM (Equations 4.1) are first simplified by neglecting all of the vertical components i.e.  $w_r$ ,  $p$ ,  $q$ ,  $\varphi$ ,  $\theta$ , and further by assuming the following:

- ❖ The origin of the body-fixed coordinate system is located at the center of mass of the vehicle.
- ❖ The vehicle is symmetric in its inertial properties.

$$\therefore M_{RB} = \begin{bmatrix} mI_{3 \times 3} & 0 \\ 0 & I_S \end{bmatrix} = \begin{bmatrix} m & 0 & 0 & 0 & 0 & 0 \\ 0 & m & 0 & 0 & 0 & 0 \\ 0 & 0 & m & 0 & 0 & 0 \\ 0 & 0 & 0 & I_{xx} & 0 & 0 \\ 0 & 0 & 0 & 0 & I_{yy} & 0 \\ 0 & 0 & 0 & 0 & 0 & I_{zz} \end{bmatrix}$$

where:

$M_{RB}$  = Inertia mass matrix;

$m$  = Rigid body mass

$I_{3 \times 3}$  = Identity matrix;  $I_S$  = Inertia tensor matrix

As a result, the simplified EOM that model the test vehicle's surge, sway and yaw dynamics are:

$$m[\dot{u} - vr] = a_{11}\dot{u} - (a_{22}vr + a_{62}rr) - F_{drag,1} + F_X \quad \dots surge$$

$$m[\dot{v} + ur] = a_{22}\dot{v} + a_{62}\dot{r} + a_{11}ur - F_{drag,2} + F_Y \quad \dots sway$$

$$I_{zz}\dot{r} = a_{26}\dot{v} + a_{66}\dot{r} - (a_{11} - a_{22})uv + a_{62}ur + F_Y l \quad \dots yaw$$

where:

$u$  = component body-fixed linear velocity in the 1 direction (surge)

$v$  = component body-fixed linear velocity in the 2 direction (sway)

$r$  = component body-fixed angular velocity in the 6 direction (yaw) = yaw rate

$I_{zz}$  = rotational mass moment of inertia about the z axis

$F_X$  = external propulsion force in the 1 direction

$F_Y$  = external propulsion force in the 2 direction

$F_Y.l$  = external turning moment about the 6 direction

Only  $I_{zz}$  is considered because the vehicle has a symmetrical structure and only translates in the horizontal plane, rotating only along the z axis. Also  $a_{26}$ ,  $a_{62}$ , which are

crossflow added mass coefficients, are neglected since the vehicle is considered to have a uniform cross-section over its length.

Therefore the final rigid body dynamics model for the test vehicle for 2DOF, obtained from simplification of equations 4.1 – 4.9, becomes:

$$\dot{u} = \frac{F_X + (m - a_{22})vr - F_{drag,1}}{(m - a_{11})} \quad (4.10)$$

$$\dot{v} = \frac{F_Y - (m - a_{11})ur - F_{drag,2}}{(m - a_{22})} \quad (4.11)$$

$$\dot{r} = \frac{F_Y l - (a_{11} - a_{22})uv}{(I_{ZZ} - a_{66})} \quad (4.12)$$

$$\dot{x} = u \cos \psi - v \sin \psi \quad (4.13)$$

$$\dot{y} = u \sin \psi + v \cos \psi \quad (4.14)$$

$$\dot{\psi} = r \quad (4.15)$$

where:

$\dot{x}$  = component global linear velocity in the 1 direction

$\dot{y}$  = component global linear velocity in the 2 direction

$\dot{\psi}$  = component global angular velocity in the 6 direction (yaw) = yaw rate

The above simplified equations are linearized and reduced to the Linear Time Invariant (LTI) form for use in a Simulink controller design model.

### 4.3 LINEARIZATION OF THE MATHEMATICAL MODEL

The linearization of the mathematical rigid body dynamics model (Equations 4.10 – 4.15) is required for easier integration of the equations of motion and is based upon the small perturbations theory and steady state conditions [38].



In steady state conditions:

$$\begin{aligned}\dot{\mathbf{u}}_0 &= \mathbf{0}; \dot{\mathbf{v}}_0 = \mathbf{0}; \dot{\mathbf{r}}_0 = \mathbf{0} \\ \mathbf{u} &= \mathbf{u}_0; \mathbf{v} = \mathbf{v}_0; \mathbf{r} = \mathbf{r}_0\end{aligned}\tag{4.16}$$

The variables are then replaced by the superposition of a steady state value and a small perturbation (increment  $\Delta$ ):

$$\begin{aligned}\dot{\mathbf{u}} &= \dot{\mathbf{u}}_0 + \Delta\dot{\mathbf{u}}; \dot{\mathbf{v}} = \dot{\mathbf{v}}_0 + \Delta\dot{\mathbf{v}}; \dot{\mathbf{r}} = \dot{\mathbf{r}}_0 + \Delta\dot{\mathbf{r}} \\ \mathbf{u} &= \mathbf{u}_0 + \Delta\mathbf{u}; \mathbf{v} = \mathbf{v}_0 + \Delta\mathbf{v}; \mathbf{r} = \mathbf{r}_0 + \Delta\mathbf{r}\end{aligned}\tag{4.17}$$

The linearization procedure further involves replacing the variables in their incremental form within the EOM while neglecting the products of the small perturbations and is completed by rewriting the EOM in a simply incremental form by subtracting the steady state components.

The equations 4.10 – 4.15 above can then be represented as:

$$(m - a_{11})\Delta\dot{u} = F_X - (a_{22} - m)(v_0\Delta r + r_0\Delta v) - D_1 u_0 \Delta u\tag{4.18}$$

$$(m - a_{22})\Delta\dot{v} = F_Y - (m - a_{11})(u_0\Delta r + r_0\Delta u) - D_2 v_0 \Delta v\tag{4.19}$$

$$(I_{ZZ} - a_{66})\Delta\dot{r} = F_Y \cdot l - (a_{11} - a_{22})(u_0\Delta v + v_0\Delta u)\tag{4.20}$$

where:

$$D_i = \text{drag force component in the } i \text{ direction} = \rho A_{P,i} C_{D,i}$$

$i$  = directions 1,2

In state space form:

$$\dot{\mathbf{x}} = \mathbf{A}\mathbf{x} + \mathbf{B}\mathbf{u}\tag{4.21}$$

where,  $\mathbf{x}$  (the state vector) =  $[\Delta u \ \Delta v \ \Delta r]^T$  and

$\mathbf{u}$  (the system input vector) =  $[F_X \ F_Y]^T$

$$A = \begin{bmatrix} -D_1 u_0 / m_1 & -(a_{22} - m) r_0 / m_1 & -(a_{22} - m) v_0 / m_1 \\ -m_1 r_0 / m_2 & -D_2 v_0 / m_2 & -m_1 u_0 / m_2 \\ -(a_{11} - a_{22}) v_0 / m_3 & -(a_{11} - a_{22}) u_0 / m_3 & 0 \end{bmatrix}$$

$$B = \begin{bmatrix} 1/m_1 & 0 \\ 0 & 1/m_2 \\ 0 & l/m_3 \end{bmatrix}; \quad m_1 = (m - a_{11}); \quad m_2 = (m - a_{22}); \quad m_3 = (I_{zz} - a_{66})$$

where A is the state matrix and B is the input matrix.

## CHAPTER 5: TEST VEHICLE EXPERIMENTS

As mentioned in the previous chapters, the proposed syringe-plunger propulsion mechanism is installed in a test vehicle for further evaluation.

### 5.1 EXPERIMENTAL SETUP

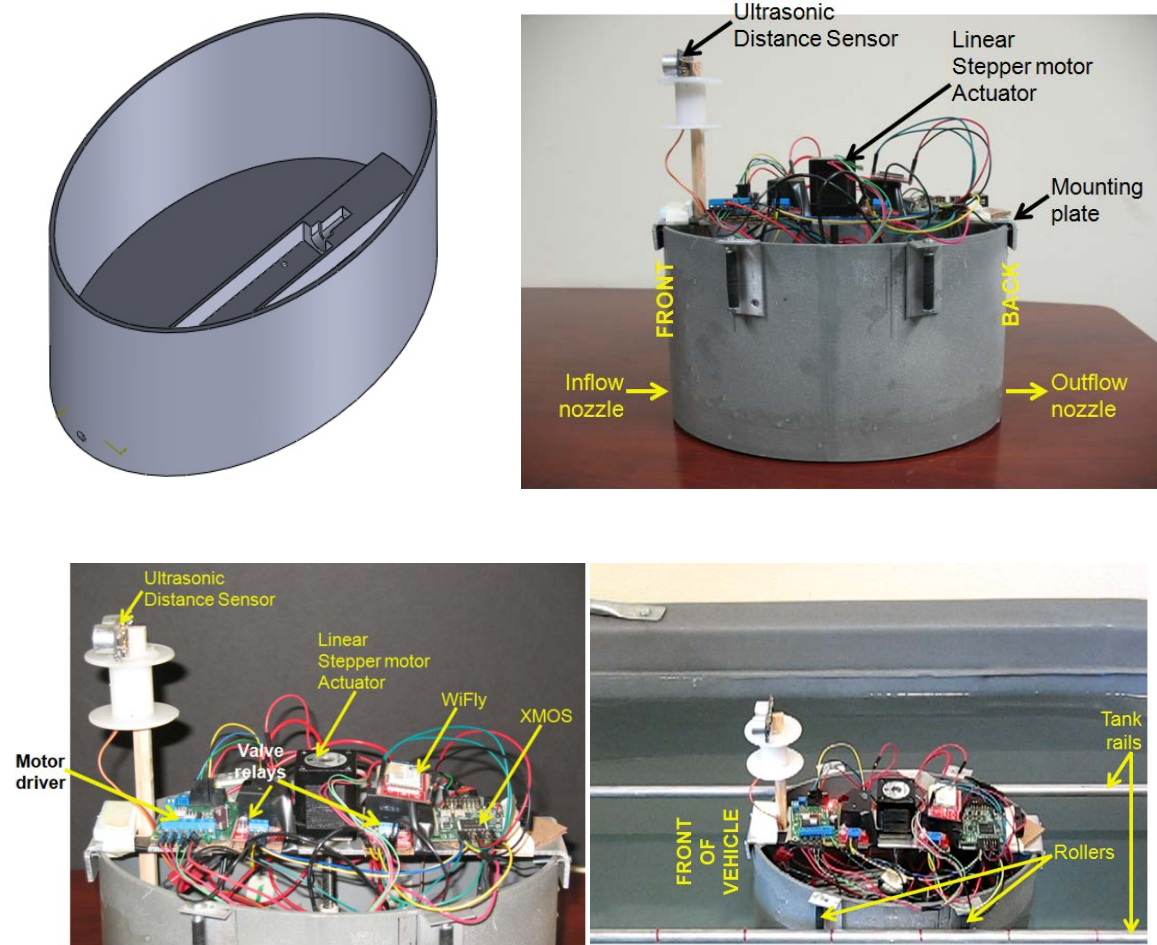


*Figure 5.1(a): Clockwise from top-left: A solid model illustration of the first generation test vehicle; Experimental setup (full side view); Experimental setup (top side view); Test vehicle in the water tank;*

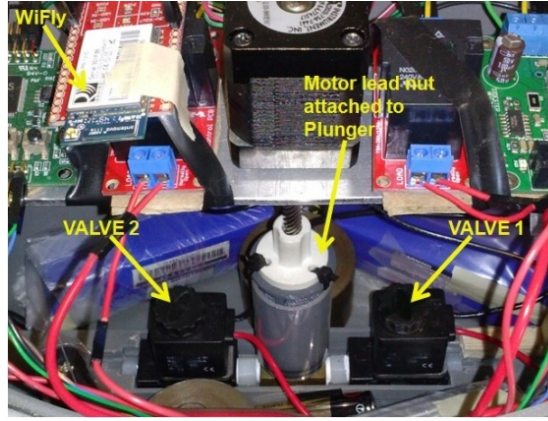


Figure 5.1(b): Experimental setup (showing the syringe, plunger and valves in the test vehicle)

### 5.1.1 VEHICLE APPARATUS OPERATION

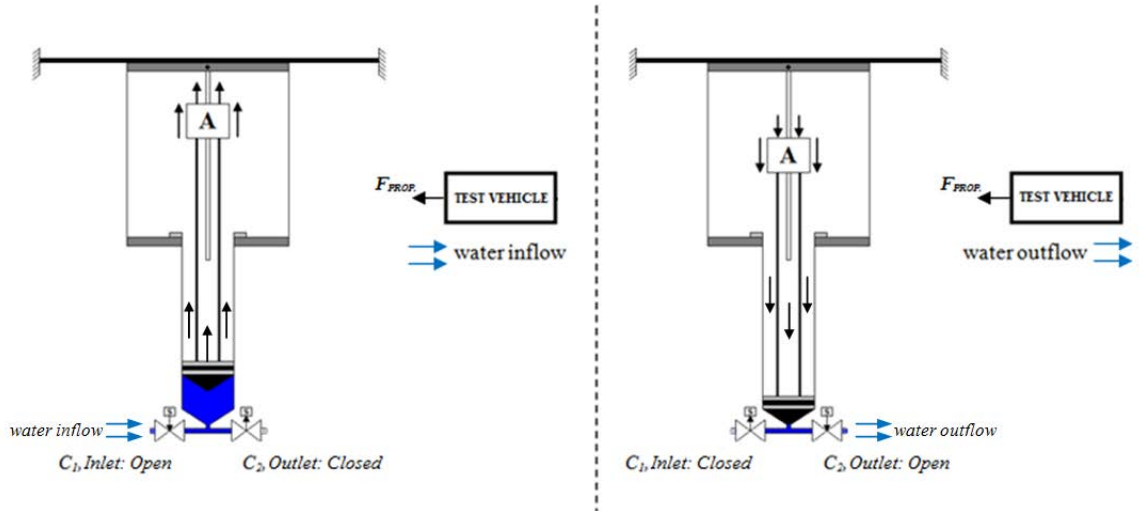


Figure 5.2: Free body force diagram for the experiments with the test vehicle

The XMOS microcontroller is used to send commands to the valve relays, motor driver, WiFly module and ultrasonic distance sensor. The valve relays open and close the solenoid valves as required during the experiments. For each set of experiments, square wave signal commands of 50% duty cycle and particular frequency are sent from the XMOS microcontroller via the stepper motor driver to the linear stepper motor actuator

to control its direction of movement, linear displacement and speed. The plunger is rigidly attached to the motor's lead nut and therefore is pulled up and pushed down the syringe barrel when the lead nut moves during the upstroke and downstroke actions respectively.

During the upstroke motion of the plunger, commands are sent to valve relays 1 and 2 to open control port  $C_1$  of valve 1 and close port  $C_2$  of valve 2 respectively. Water is drawn into the syringe barrel through the vehicle's inflow nozzle and port  $C_1$ . Subsequently, during the downstroke motion of the plunger, commands are sent to valve relays 1 and 2 to close control port  $C_1$  and open port  $C_2$  respectively. Water is pushed out of the syringe barrel through the vehicle's outflow nozzle and port  $C_2$ . Repeated upstroke and downstroke motions of the plunger, causing water to be drawn into and pushed out of the syringe, result in forward propulsion of the vehicle by the induced forces as illustrated in Figure 5.2.

A WiFly wireless radio is connected and programmed to communicate with the XMOS microcontroller to allow the user to remotely operate the system, i.e. the motor, valve relays and ultrasonic sensor, as required during experiments. A remote system is required because external cable connection would interfere with the vehicle dynamics and movement as well as the authenticity of the sensor measurements. The ultrasonic distance sensor is used to return position data (in mm) and the time elapsed between subsequent position measurements (in milliseconds) as the vehicle moves forward in the water tank. The position data indicates the vehicle's position in the tank relative to the end of the tank where an artificial wall/barrier is placed (Figure 5.3).



*Figure 5.3: The test vehicle in the water tank (full view)*

### **5.1.2 VEHICLE APPARATUS COMPONENTS AND SOFTWARE**

The apparatus used for the experiments with the test vehicle comprises of the following hardware and software components:

- ❖ Haydon Kerk linear stepper motor actuator (NEMA 8, 2.5V 0.49A Bipolar, part No: E21H4U-2.5-900)
- ❖ Haydon Kerk linear stepper motor actuator (NEMA 14, 2.33V 2A Bipolar, double stack, part no.: E35M4AG-2.33-900)
- ❖ Pololu DRV8825 Stepper Motor Driver (Bipolar Microstepping, 8.2–45V, 2.2A)
- ❖ Probotix Stepper Motor Driver (Bipolar Microstepping Chopper driver, 8–32V, 0.5-2.5A current limiting)
- ❖ Syringe barrel and Plunger (10ml and 60ml size)
- ❖ XMOS XK-1A microcontroller and xTIMEcomposer Studio Development Environment/Software
- ❖ Arduino Uno ATmega328 microcontroller board and Arduino programming platform

- ❖ 2 Normally-closed Solenoid valves (12V 6W)
- ❖ 2 Single-side stable TTL (Transistor–transistor logic) relays (TF2-5V)
- ❖ 2 Sparkfun Beefcake Relay Control Kits (5V)
- ❖ Sparkfun WiFly GSX module
- ❖ Parallax PING)))<sup>TM</sup> Ultrasonic Distance Sensor (range: 2 cm to 3 m)
- ❖ One 22.2V, two 12V and one 5V DC power supply batteries
- ❖ 2' x 2' x 6' Oblong Water tank

## **5.2 VEHICLE APPARATUS AS A MECHATRONIC SYSTEM**

The experimental setup for the test vehicle (Figure 5.1) can be divided into 3 categories:

1. The mechanical subsystem
2. The electrical subsystem
3. The software and communication subsystem

In the following, the design, fabrication and assembly of each of these are discussed as well as the challenges involved in getting each subsystem, and finally the vehicle setup to function properly.

### **5.2.1 THE MECHANICAL SUBSYSTEM**

This part of the apparatus consists mainly of the test vehicle body, the linear stepper motor actuator, the syringe barrel and plunger, the motor lead screw and nut and the mounting plate.

The test vehicle body and plunger are designed using SolidWorks 3D CAD software and produced using an FDM 3D printing machine. Several iterations of the test

vehicle design, two versions are shown in Figure 5.4, are done to ensure optimum installation of the propulsion mechanism, including the solenoid valves, in the test vehicle while maintaining a smooth outer body surface.

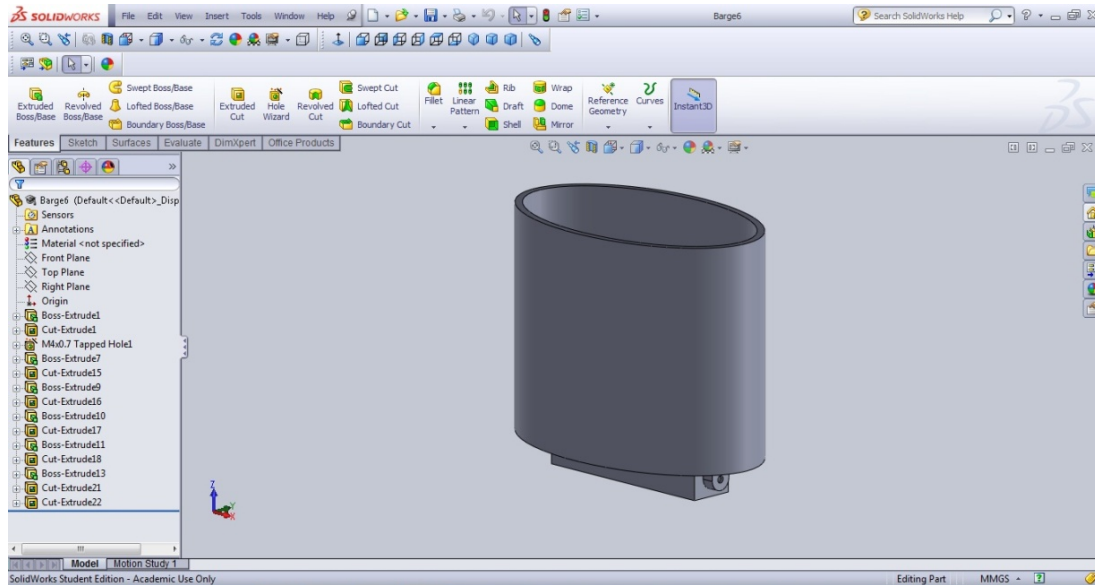


*Figure 5.4(a): Test vehicle SolidWorks design, Version 1*

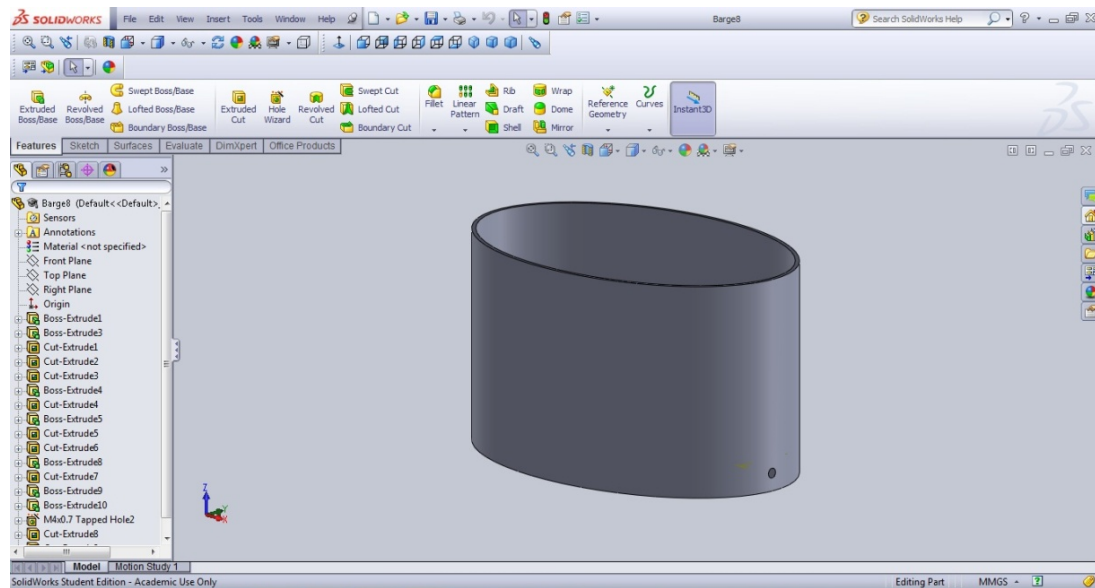


*Figure 5.4(b): Test vehicle SolidWorks design, Version 2*



With the main aim to keep the overall weight of the test vehicle and the power requirements of the propulsion system as low as possible, to start with, a small (NEMA 8, 43g, 2.45W) linear stepper motor actuator is used (Figure 5.5). However despite the motor's high load capacity and with the maximum possible water control volume used, the thrust produced can only move the vehicle forward at a speed of approximately 0.5cm/s. Therefore, the motor is replaced with a faster one to increase the mass flow rate of the water and as a result the thrust output of the system. This faster motor (NEMA 14, 240g, 9.1W) is however bigger, heavier and has higher power consumption and thus leads to a number of system/apparatus design changes.

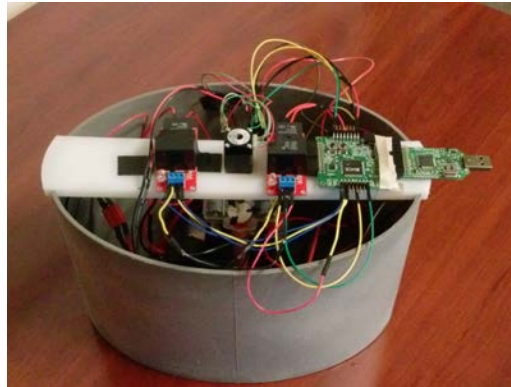


*Figure 5.5: Initial apparatus with small motor, 10ml syringe and plastic mounting plate*

Three iterations of the plunger size and design (Figure 5.6) are done to ensure rigidity of its linkage to the motor's lead nut and to allow an increase of the water control volume drawn into and out of the syringe during operation. Increase in the water control volume results in increase of the maximum mass flow rate and hence the thrust output of

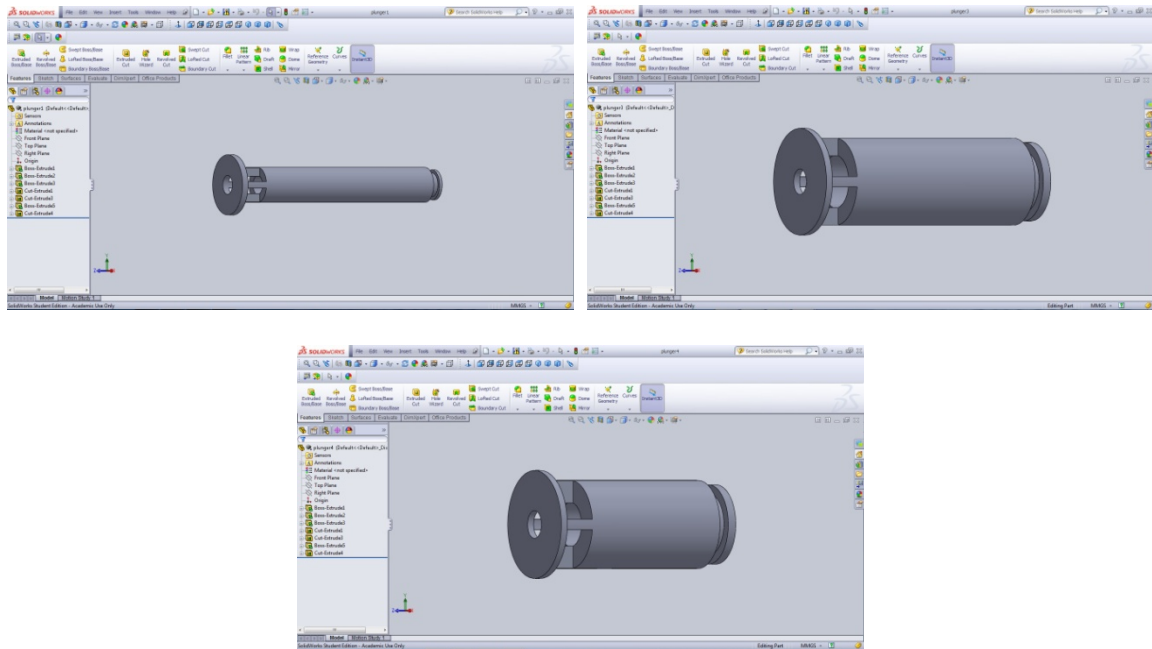


*Figure 5.6: Plunger SolidWorks designs, Clockwise: Versions 1 – 3*

the system. Also, the length of the motor's lead screw restricts the water volume drawn and ejected during operation and is therefore trimmed in-line with the changes to the plunger size and design.

Two different design materials are used to fabricate the mounting plate (Figure 5.5 and Figure 5.1). Both cases are designed using SolidWorks 3D CAD software. The first design is initially implemented with the small size motor and is fabricated from a light-weight, machinable, high strength plastic. It is observed though that with the larger motor mounted on the plate, this material flexes a lot when the system is in operation and the motor is pulling and pushing the plunger. This flexing translates to a considerable loss in the thrust achievable with each plunger movement. To counter this, the second design is fabricated from metal, specifically an aluminum (Alloy 6061) 1/8" thick bar, which is more rigid.

Further, since the experimental setup is top-heavy, more so with the bigger motor, additional ballast weights are added inside the test vehicle together with the power supply batteries to balance the vehicle in the water tank. In addition, during operation it is observed that the propulsion forces acting at the front and back of vehicle are slightly skewed and cause the vehicle to veer from the expected straight line trajectory. For this reason, parallel rails are installed along the length of the water tank (Figure 5.1.b) to keep the vehicle in a straight forward track. This also ensures that the signals from the ultrasonic distance sensor mounted at the front of the vehicle are orthogonal to the wall at the end of the tank and therefore provide an accurate distance measurement. To keep the vehicle from stalling even when it bumps into the rails in the tank as it moves forward, four rollers are fabricated and mounted onto the sides of the vehicle body.

## 5.2.2 THE ELECTRICAL SUBSYSTEM

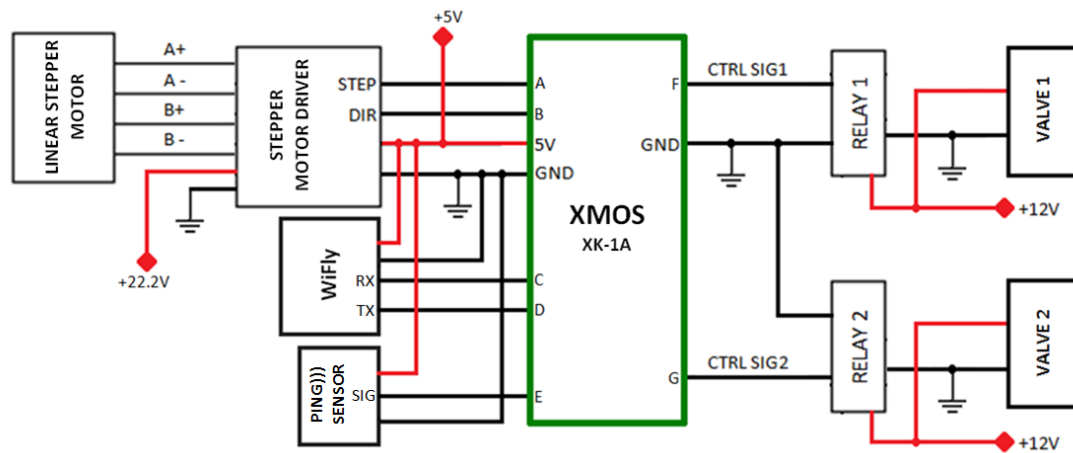


Figure 5.7: A schematic of the test vehicle electrical circuit

The electrical subsystem is comprised of the circuit shown in Figure 5.7. The ports A-G of the XMOS XK-1A microcontroller are one bit general-purpose digital

input/output ports. These I/O ports provide output signals at 3.3V with a maximum current draw of 200mA.

Relays are electrically operated switches used where it is necessary to control a high-power component/circuit with a low-power signal while ensuring complete electrical isolation between the control and controlled circuits. In this case, the low-power signals are those from the microcontroller (3.3V each) and the high-power components are the normally-closed solenoid valves which require 12V to open/operate. A high signal from the microcontroller to the relays causes them to close the high-power circuit which in turn opens the valves. A low signal from the microcontroller causes the relays to open the high-power circuit and close the valves.

Initially the system consists of the microcontroller, the linear stepper motor, the stepper motor driver, the 2 Single-side stable TTL relays (TF2-5V: 5V, 16mA) (Figure 5.8) and the 2 solenoid valves. Both relays/solenoid valves are supplied by the same 12V (2200mAh) battery while the stepper motor is supplied by a separate 12V (2200mAh) battery. A control program is used to test the operation of the motor and valves and to determine the actual speed and load capacity of the motor with the apparatus design.

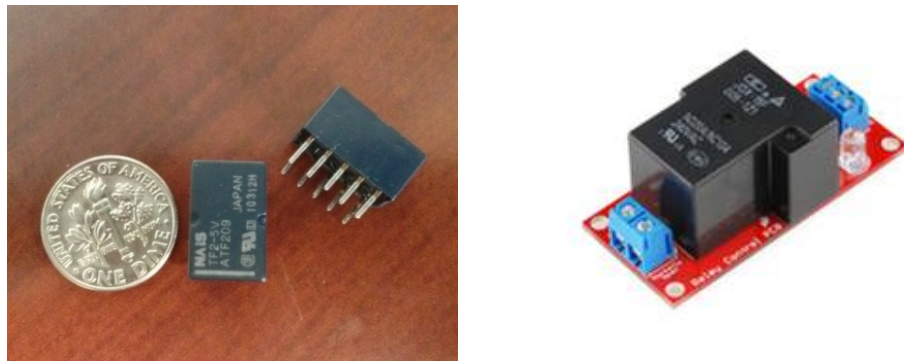


*Figure 5.8: Left: Single-side stable TTL relays (TF2-5V); Right: Sparkfun Beefcake Relay Control Kit (5V)*

The basic system is improved in several ways to make it more robust. The power supply to each of the relays is decoupled so they are each supplied by separate 12V batteries to make certain that they each receive the maximum possible power to operate the valves. Also, a Bipolar Junction Transistor (BJT) circuit is used in between the XK-1A output ports and the relays to amplify the voltage of the signal being received by the relays.

Finally, a new set of valves and different types of relays is assessed and ultimately, a pair of a different type of relay (Figure 5.8) (2 Sparkfun Beefcake Relay Control Kits) and a replacement pair of valves are chosen for testing with the microcontroller. These relays have higher power capacity plus better isolation capability and it is observed that with this new set of components the system operates smoothly.

Another challenge encountered with this system is observed with the implementation of the larger motor mentioned in section 5.2.1 above with the Pololu DRV8825 Stepper Motor Driver (Figure 5.9). The motor-lead nut-plunger subsystem vibrates during operation, making a kicking sound and is also observed to be missing steps during operation as the plunger moves up and down the syringe barrel.

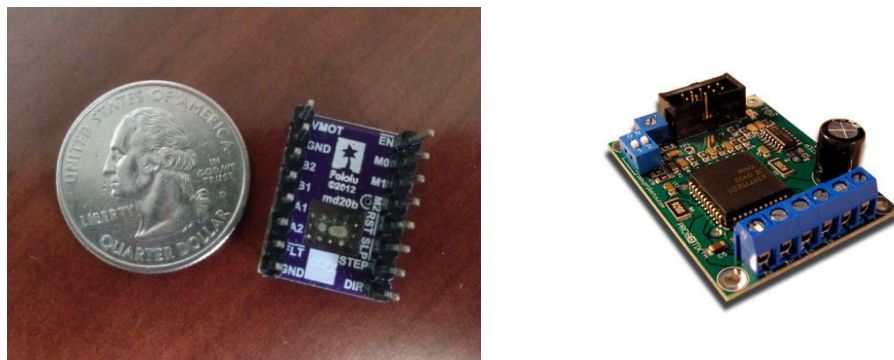


*Figure 5.9: Left: Pololu DRV8825 Stepper Motor Driver; Right: Probotix Stepper Motor Driver*

Again, several steps are taken and tests done to troubleshoot this issue and it is resolved by implementing a different stepper motor driver (Figure 5.9), the Probotix Stepper Motor Driver, which has a higher power capacity and better capability at chopping/limiting the motor current.

### **5.2.3 THE SOFTWARE AND COMMUNICATION SUBSYSTEM**

This part of the apparatus consists mainly of the XMOS XK-1A microcontroller and xTIMEcomposer Studio Development Environment/Software, the Sparkfun WiFly GSX module and the Parallax PING)))<sup>TM</sup> Ultrasonic Distance Sensor.

The XMOS XK-1A microcontroller and XMOS Development Environment/Software are used as the primary embedded controller and programming software in this work. XMOS technology is chosen for use in this project as it is the main platform in use for unmanned vehicles and systems research by the DU<sup>2</sup>SRI group. The XMOS microcontrollers are able to run the complex computational tasks required for intelligent, autonomous behavior while at the same time monitoring several sensor systems by using event-driven multi-threaded processors [39].

The XK-1A is a low cost development board that comprises a single XS1-L1 device, 128Kbytes SPI interface to FLASH memory, 24 I/O pins and is clocked at 20MHz by a crystal oscillator on the board [40]. The XK-1A board can be powered from a USB connection using an XTAG-2 debug adapter or by an external 5V power supply (Figure 5.10). It is programmed through the XTAG-2 in an Eclipse-based environment known as xTIMEcomposer Studio supplied by XMOS.



*Figure 5.10: XK-1A board and XTAG-2 debug adapter*

The WiFly Wi-Fi module is connected and programmed to communicate with the XK-1A microcontroller board to allow the user to remotely operate the motor, valve relays and ultrasonic distance sensor as required during experiments. The user interface can be setup via a TELNET connection to the WiFly's IP address and port. Figure 5.11 shows the user interface. The information returned to the user through this interface for this experiments includes: position data (in mm) and the time elapsed between subsequent measurements (in milliseconds) from the ultrasonic distance sensor, the state and direction of movement of the linear stepper motor actuator (and plunger) as well as the speed of the plunger for both the upward and downward strokes.

A single I/O pin is used to trigger an ultrasonic burst (well above human hearing) from the PING)))<sup>TM</sup> sensor (Figure 5.12) and then "listen" for the echo return pulse when the ultrasonic signal reaches the wall. The sensor is programmed to measure the time required for the echo return and then return this value to the microcontroller as a variable-

width pulse via the same I/O pin. This time data is the converted in the XC program into position data (in mm) by incorporating the speed of sound in air.

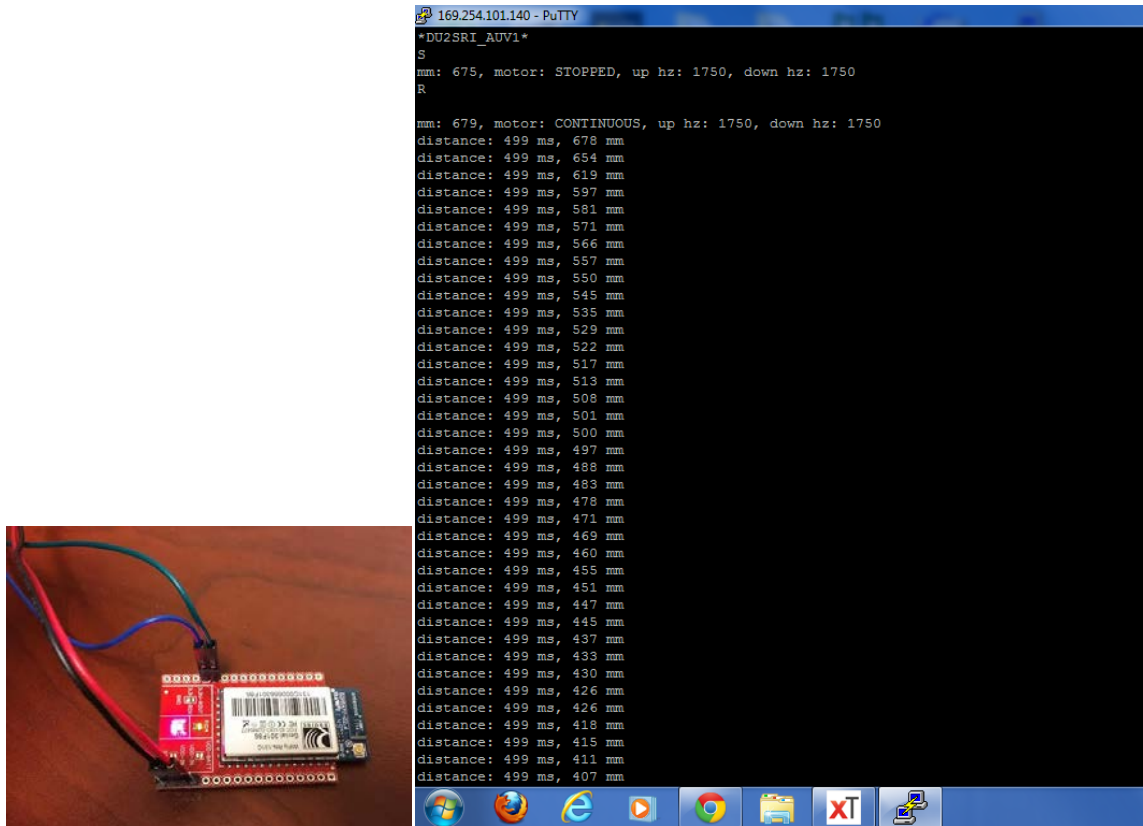


Figure 5.11: Left: Sparkfun WiFly GSX module; Right: The user interface



Figure 5.12: Parallax PING)))™ Ultrasonic Distance Sensor



## **CHAPTER 6: TEST VEHICLE EXPERIMENTAL AND SIMULATION**

### **RESULTS**

As described in Section 5.1, for these experiments the microcontroller is used to send commands to the valve relays, motor driver, WiFly and ultrasonic distance sensor.

Signal commands of particular frequency are sent from the XK-1A microcontroller via the motor driver to the motor to control its direction of movement, linear speed and linear displacement. Experiments are performed for various actuation sequences where the linear speed of the plunger movement is varied from 1.191cm/s to 2.680cm/s by changing the frequency of the signals sent from the microcontroller. This is done to determine the influence of the type of flow (as described by the Reynolds number), through the vehicle inflow and outflow nozzles, on the thrust output of the mechanism and vehicle speed. As in the direct thrust measurement experiments discussed in Chapter 3, experiments for three different actuation sequences/cases are carried out.

1. **CASE 1:** Equal plunger upstroke and downstroke speed.
2. **CASE 2:** Plunger upstroke speed faster than the downstroke speed. The upstroke speed is kept constant at 2.680cm/s while the downstroke speed is increased from 1.191cm/s to 2.382cm/s for each consecutive set of experiments.
3. **CASE 3:** Plunger downstroke speed faster than the upstroke speed. The downstroke speed is kept constant at 2.382cm/s while the upstroke speed is increased from 1.191cm/s to 2.085cm/s for each consecutive set of experiments.

The disparity in the maximum upstroke and downstroke plunger speeds for cases 2 and 3 above is due to hardware failures and challenges with the linear actuator during the course of these experiments. Each experiment begins with the test vehicle positioned at one end of the testing tank. Once the water in the tank has completely settled, the linear actuator, valves and ultrasonic distance sensor are activated to run continuously. The plunger starts to move upwards and then downwards drawing and pushing 20ml of water into and out of the syringe barrel.

These actions provide propulsive forces, as described in Section 5.1.1, to the vehicle causing it to move forward. The vehicle gains momentum and accelerates and once it gets to two-thirds of the way along the tank the actuator (i.e. plunger) and valves are powered off/stopped. The ultrasonic sensor is left running to keep collecting position and time data until the vehicle comes to a forced stop at the far end of the tank and then is also deactivated. This marks the end of the experiment. The experimental data is extracted from the user interface and initially saved in MS Excel for processing. All experiments are run/conducted at least four times.

In the following, plots of the average vehicle position vs. time curves (with one standard deviation error bars) for all the experiments are presented.

### Average Vehicle Position vs. Time Curves (with the actuator running)

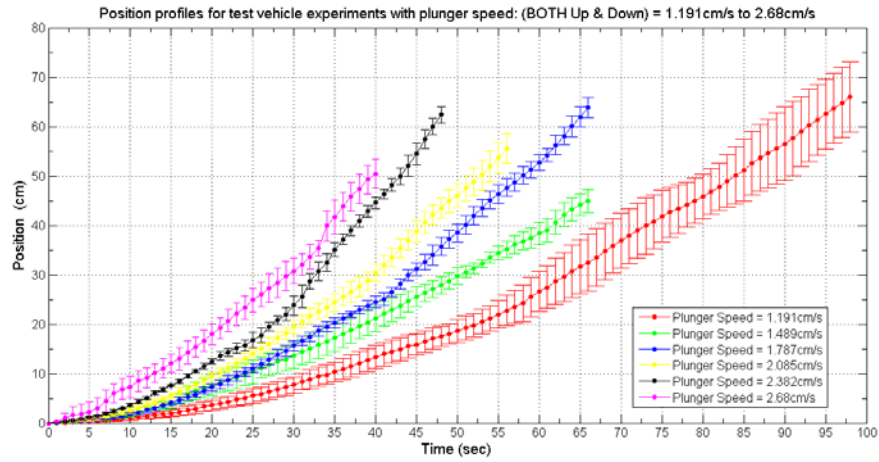


Figure 6.1 (a): CASE 1 Experiments: Average vehicle position vs. time curve

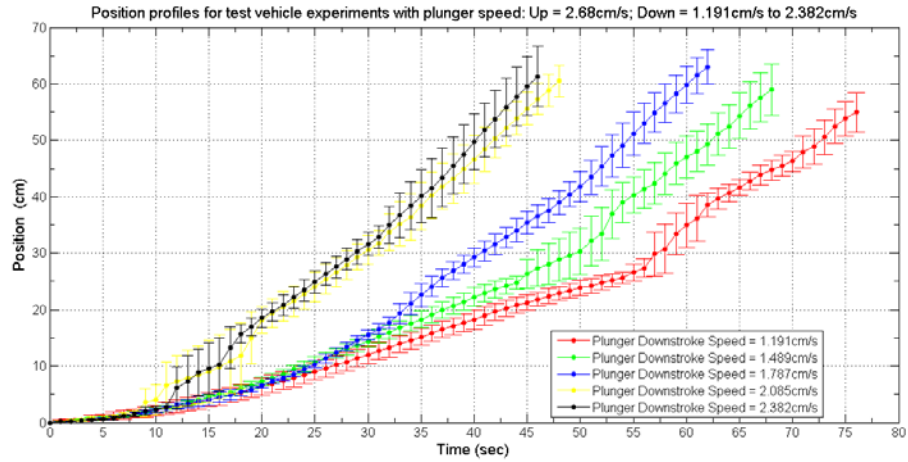


Figure 6.1 (b): CASE 2 Experiments: Average vehicle position vs. time curve

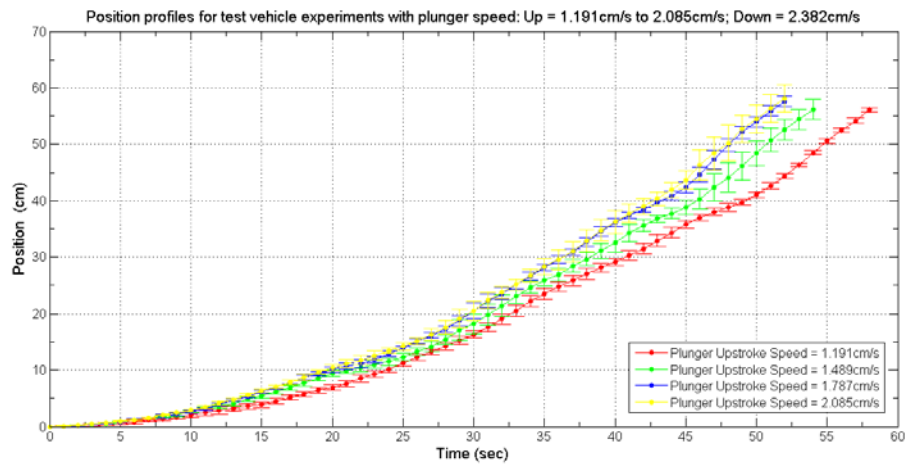
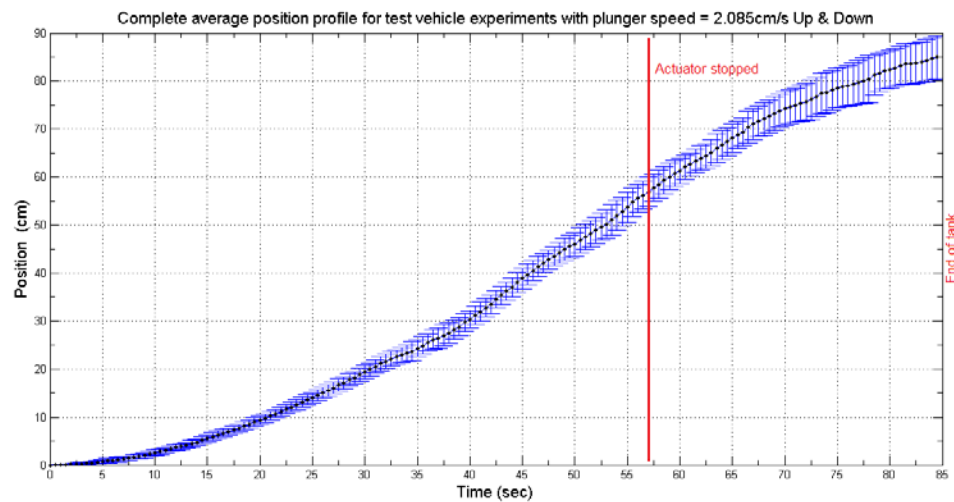


Figure 6.1 (c): CASE 3 Experiments: Average vehicle position vs. time curve

## 6.1 DATA ANALYSIS

Data analysis for each experiment begins with plotting the vehicle's the raw position data against time for each of the runs. Next, linear interpolation in Matlab is performed on each of the four or more data sets at the sampling time of 0.5s and the average vehicle position vs. time curve is obtained for each experiment. As an example, Figure 6.2(a) shows a plot of the average vehicle position vs. time curve for the experiment where the plunger speed is 2.085cm/s for both the upstroke and downstroke.

Next, the velocity profile, Figure 6.2(b), is plotted from differentiation of the average vehicle position data obtained above with respect to time. This plot is erratic as it shows the fluctuation in the velocity of the vehicle every 0.5s. Therefore, for useful analysis this initial velocity profile plot is smoothed by considering the change in the vehicle's velocity every 2s instead, i.e. after every three data points. Figure 6.3 shows this velocity plot for the portion of the experiment when the actuator is running.



*Figure 6.2(a): Average vehicle position vs. time curve: Plunger speed = 2.085cm/s for both Upstroke and Downstroke*

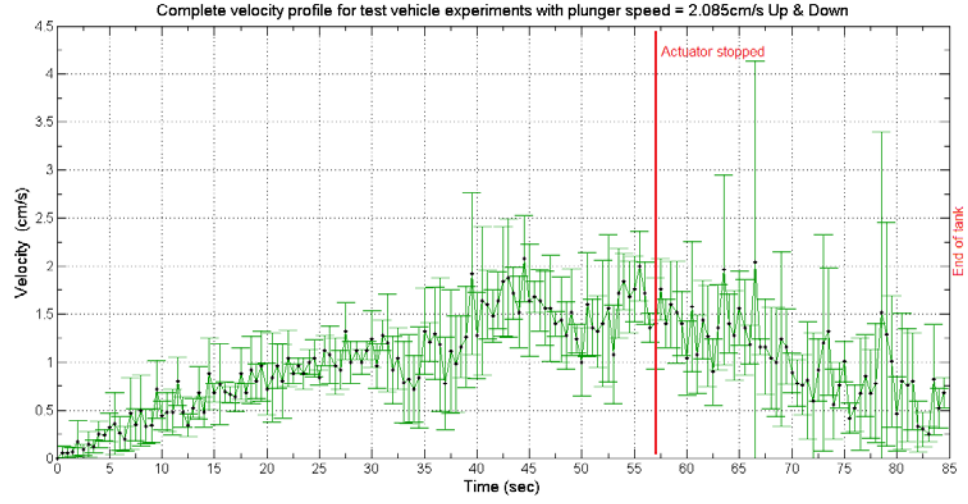


Figure 6.2(b): Vehicle velocity curve: Plunger speed = 2.085cm/s for both Upstroke and Downstroke

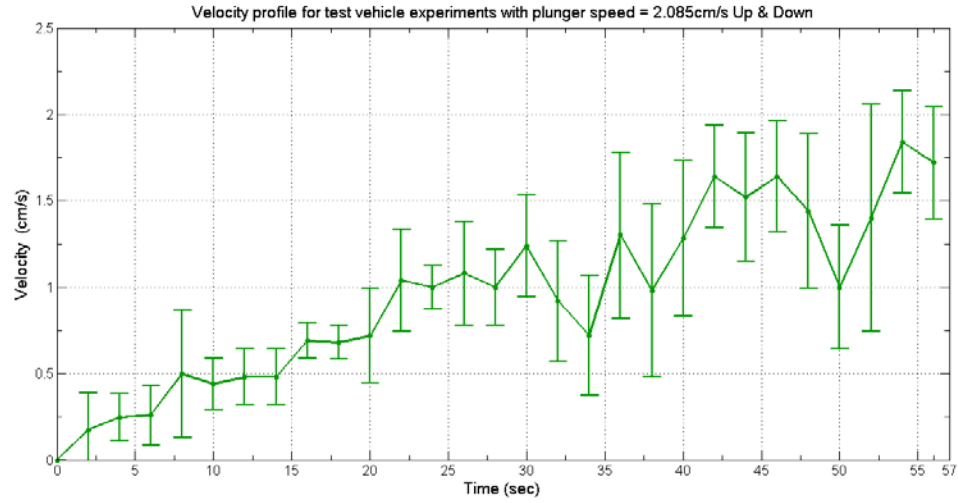


Figure 6.3: Vehicle velocity curve (smoothed): Plunger speed = 2.085cm/s for both Upstroke and Downstroke

For 1 DOF motion, the rigid body dynamics model equations 4.10 – 4.15 in Section 4.2.4 for the vehicle reduces to Equation 6.1 and 6.2 below.

$$\dot{\mathbf{u}} = \frac{F_X - F_{drag,x}}{(M - a_{11})} \quad (6.1)$$

$$\dot{\mathbf{x}} = \mathbf{u} \quad (6.2)$$

$$F_{drag,x} = \frac{1}{2} C_D \rho A_{P,x} V_v^2 \quad (6.3)$$

where:

$u$  = component body-fixed linear velocity in the x direction

$F_X$  = external propulsion force in the x direction

$F_{drag,x}$  = drag force on the vehicle in the x direction

$M$  = total mass of the vehicle

$a_{11}$  = added-mass coefficient

$\dot{x}$  = component global linear velocity in the 1 direction

$A_{P,x}$  = projected cross-sectional area normal to the direction of the drag force

$\rho$  = mass density of water at room temperature

$V_v$  = vehicle velocity;  $C_D$  = drag coefficient

Equations 6.1 – 6.3 are used at this point to create a non-linear dynamics simulation model in Simulink (Figure 6.4) with the experimental velocity and acceleration data to model the resultant constant propulsive force,  $F_X$  produced by the mechanism for each experiment. This is done by combining the maximum drag force achieved and the force due to acceleration ( $m\dot{u}$ ) at the point when the propulsion system is powered off and the test vehicle starts to decelerate. This model is then used to estimate the speed performance of the test vehicle. Example calculations for the 2.085cm/s upstroke, 2.085cm/s downstroke experiment are presented below.

$$V_v = 1.78\text{cm/s}; \rho = 998.2\text{kg/m}^3; C_D = 0.4; A_{P,l} = 0.0176\text{m}^2; \mathbf{F_D = 0.0011N}$$

$$\dot{u} \approx 0; M = 3.69\text{kg}; a_{11} = 1.3717\text{kg}; m = 2.3183\text{kg}; \mathbf{m\dot{u} = 0}$$

$$\therefore \mathbf{F_X = 0.0011N}$$

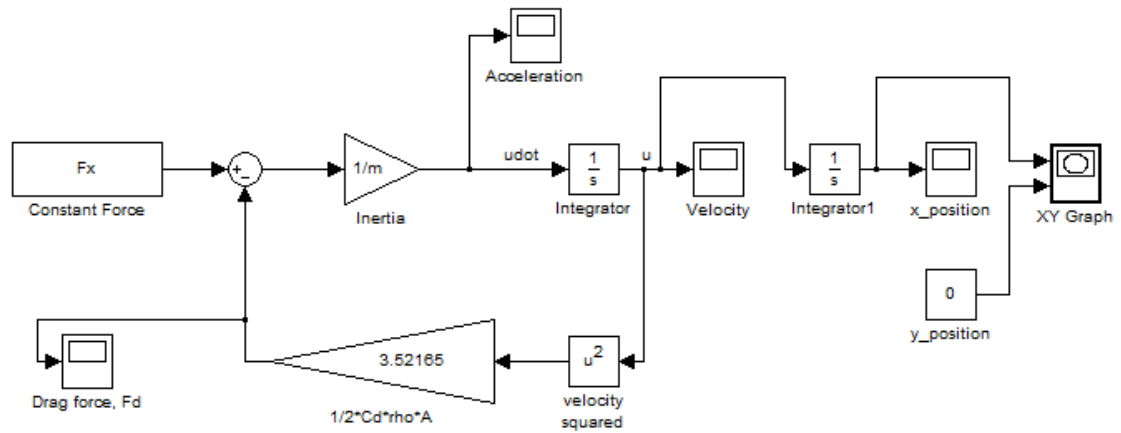


Figure 6.4: SIMULINK Non-linear test vehicle dynamics model

The position and velocity profiles of the vehicle for the constant force,  $F_x = 0.0011\text{N}$ , model obtained from simulation are shown alongside the plots produced from the experimental data in Figures 6.5(a and b).

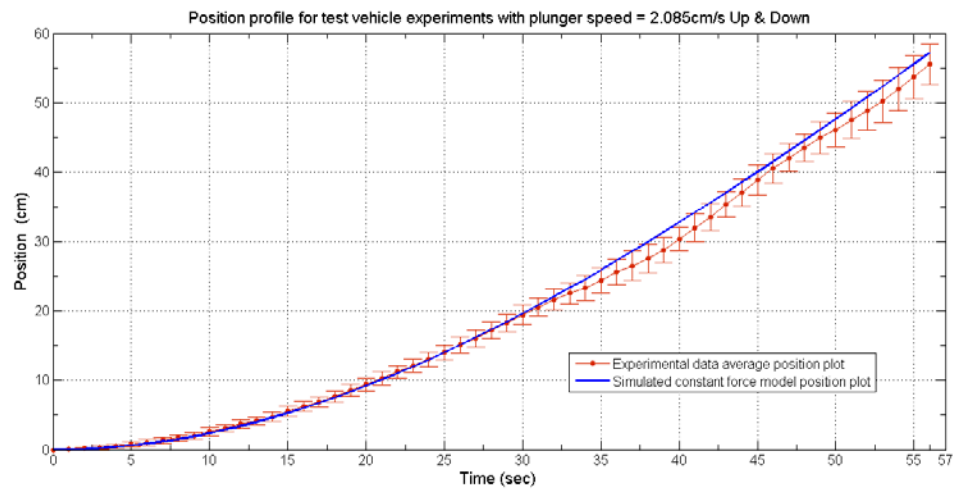
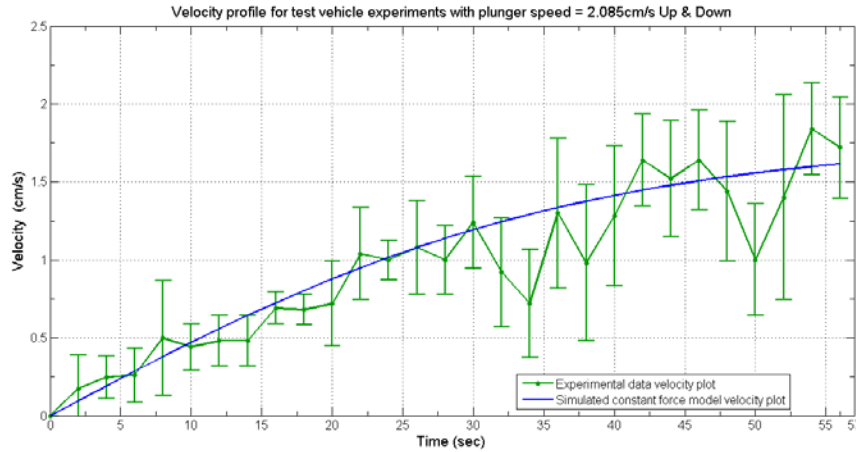


Figure 6.5(a): Position profile of the vehicle for the constant force model: Plunger speed = 2.085cm/s for both Upstroke and Downstroke



*Figure 6.5(b): Velocity profile of the vehicle for the constant force model:  
Plunger speed = 2.085cm/s for both Upstroke and Downstroke*

From Figure 6.5(a) it is observed that the vehicle's position plot obtained from the experimental data follows the simulated curve fairly closely, with the simulated curve being within one standard deviation of the experimental data plot. This presents a good basis for evaluation and implies that the effect of the rails in the water tank as well as the rollers attached on the test vehicle body on the movement of the vehicle and measurement of its position in the tank during experiments is minimal. Also, as shown in Figure 6.5(b), the simulated velocity curve for the vehicle is generally within one standard deviation of the experimental data plot.

In the following, the test vehicle position and velocity profile curves showing the simulation constant force models for all the experiments are presented (Figures 6.6 – 6.8). A similar trend as with the plots in Figure 6.5 (a and b) above is observed. The analysis outlined above is done for all the experiments and in the end enables comparison of the resultant constant thrust output of the propulsion mechanism as well as the speed of the vehicle for each of the three actuation cases tested. This comparison is presented in graphical form in Figure 6.9(a) and Figure 6.9(b).



## CASE 1 EXPERIMENTS

### Test Vehicle Position and Velocity profile curves: Showing the Constant Force Models

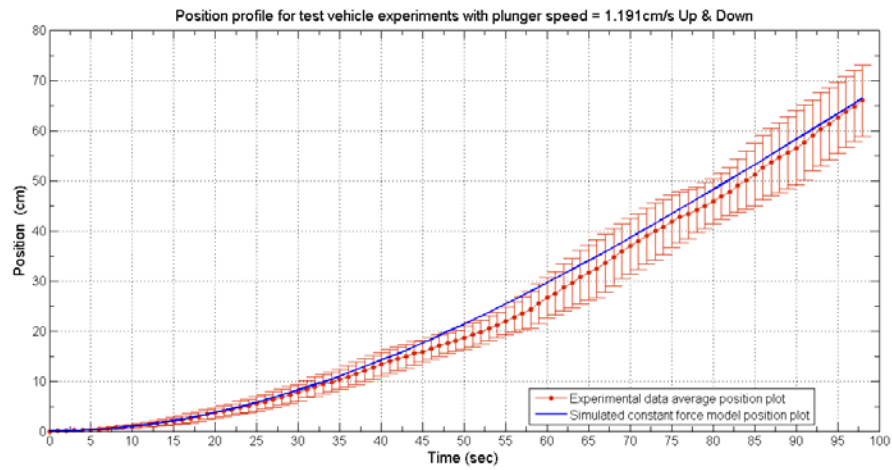


Figure 6.6 (a.1): Position plot: Plunger Speed = 1.191 cm/s both Up and Down

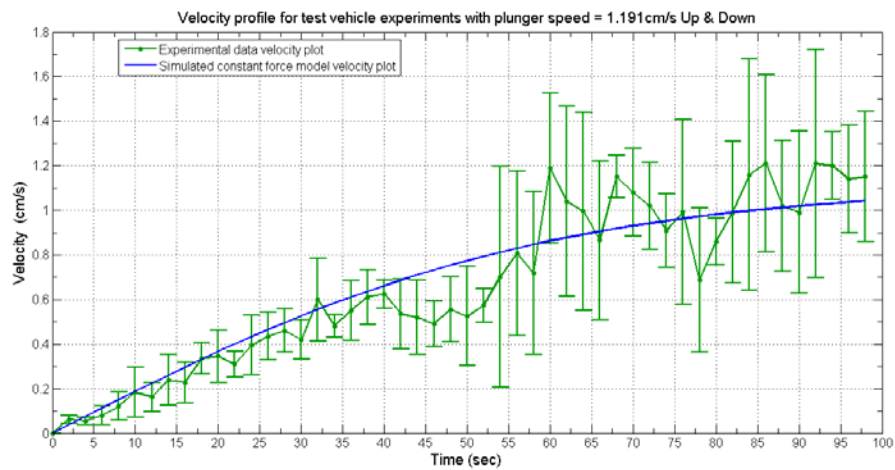


Figure 6.6 (a.2): Velocity plot: Plunger Speed = 1.191 cm/s both Up and Down

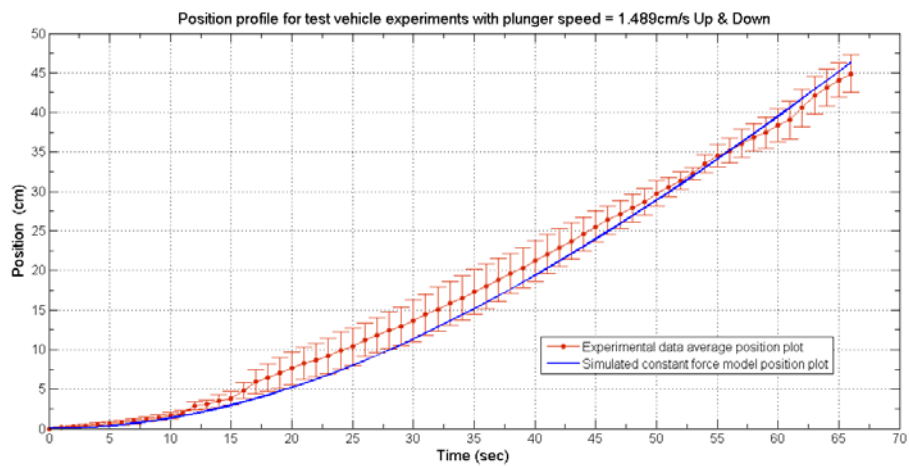


Figure 6.6 (b.1): Position plot: Plunger Speed = 1.489 cm/s both Up and Down

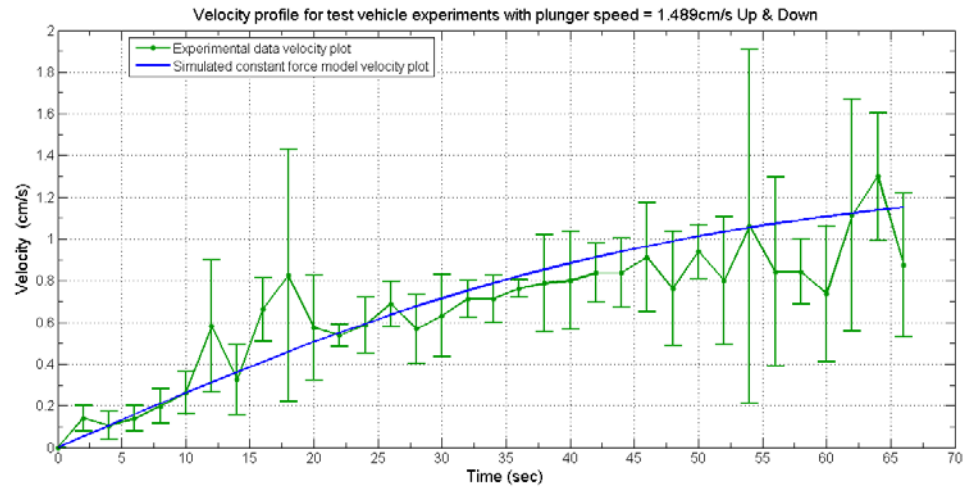


Figure 6.6 (b.2): Velocity plot: Plunger Speed = 1.489cm/s both Up and Down

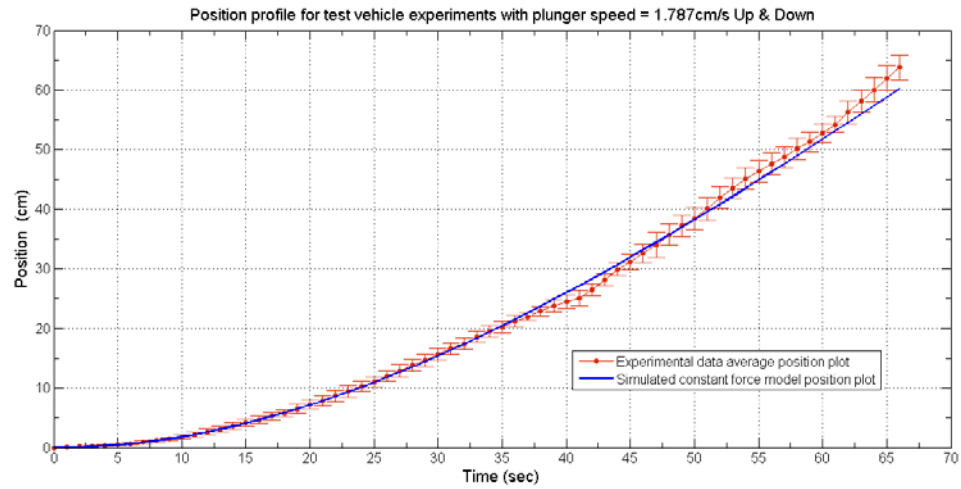


Figure 6.6 (c.1): Position plot: Plunger Speed = 1.787cm/s both Up and Down

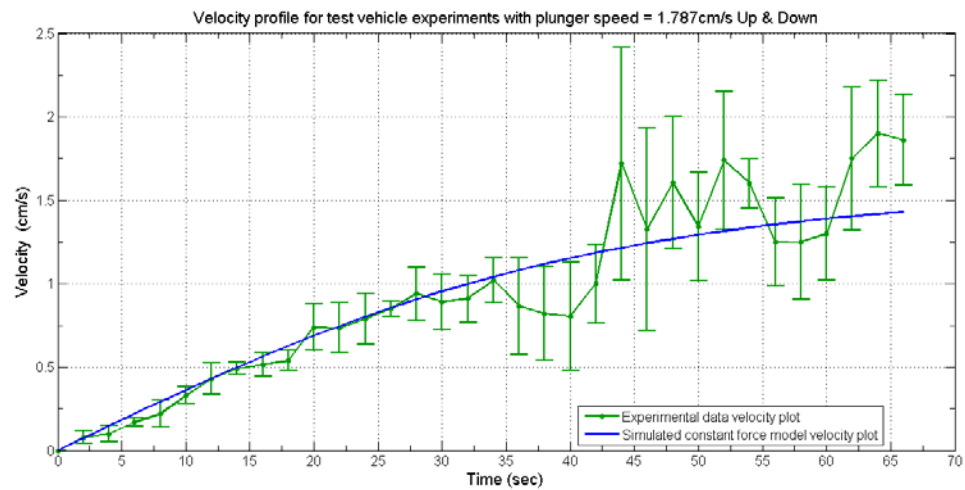


Figure 6.6 (c.2): Velocity plot: Plunger Speed = 1.787cm/s both Up and Down

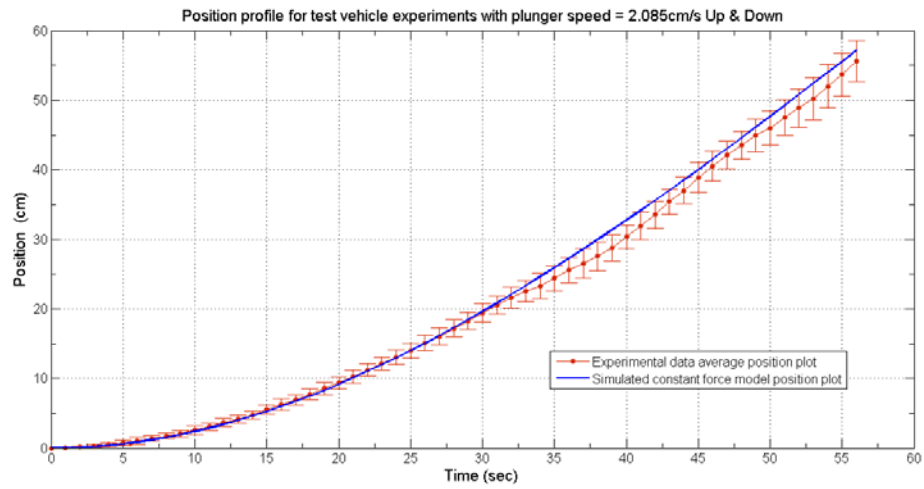


Figure 6.6 (d.1) Position plot: Plunger Speed = 2.085cm/s both Up and Down

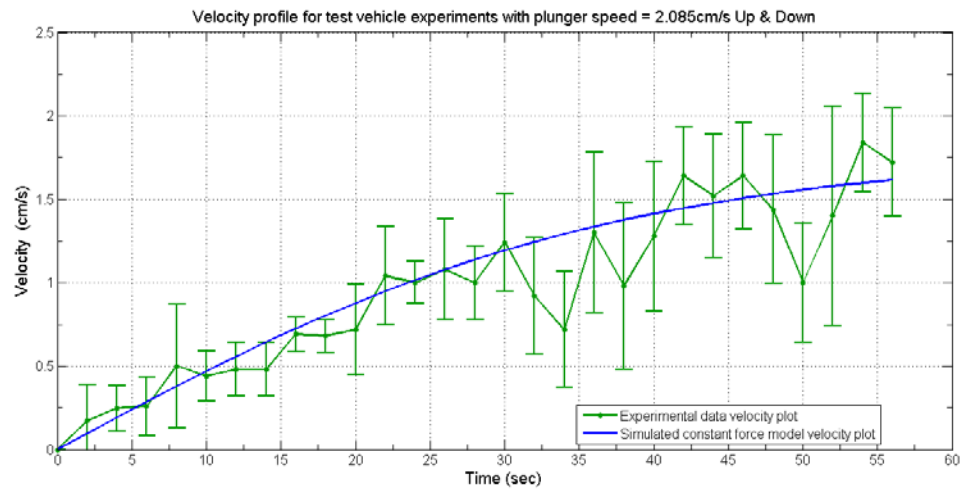


Figure 6.6 (d.2): Velocity plot: Plunger Speed = 2.085cm/s both Up and Down

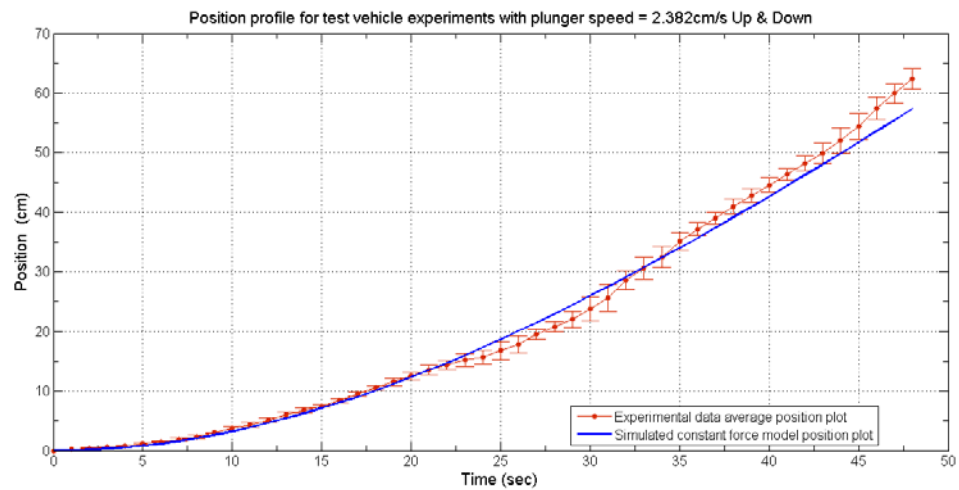


Figure 6.6 (e.1): Position plot: Plunger Speed = 2.382cm/s both Up and Down

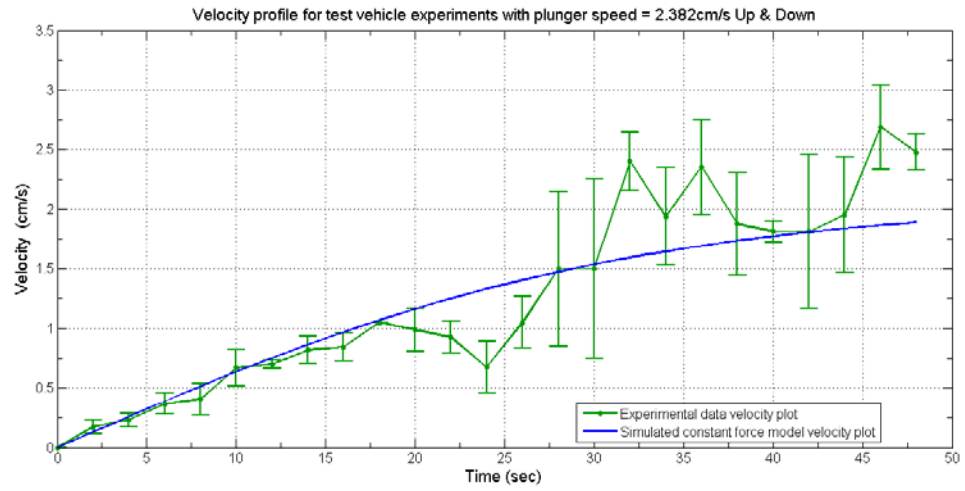


Figure 6.6 (e.2): Velocity plot: Plunger Speed = 2.382cm/s both Up and Down

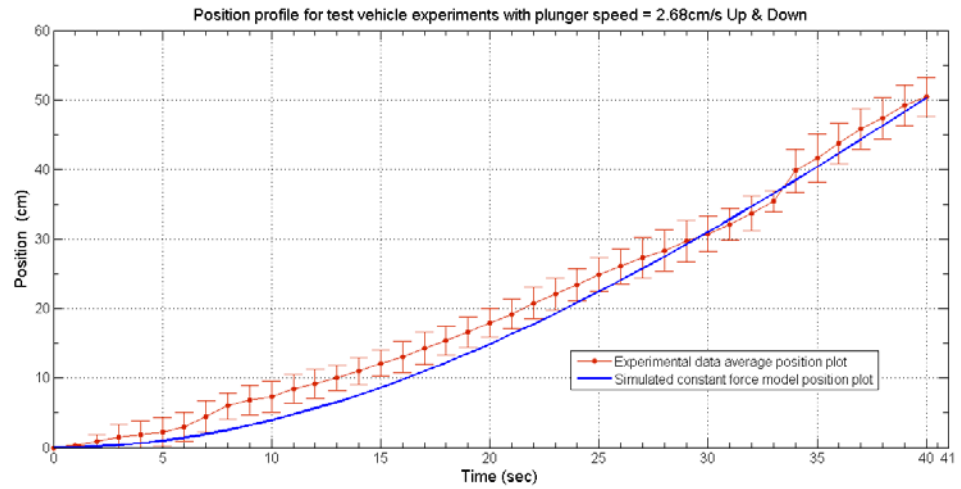


Figure 6.6 (f.1): Position plot: Plunger Speed = 2.68cm/s both Up and Down

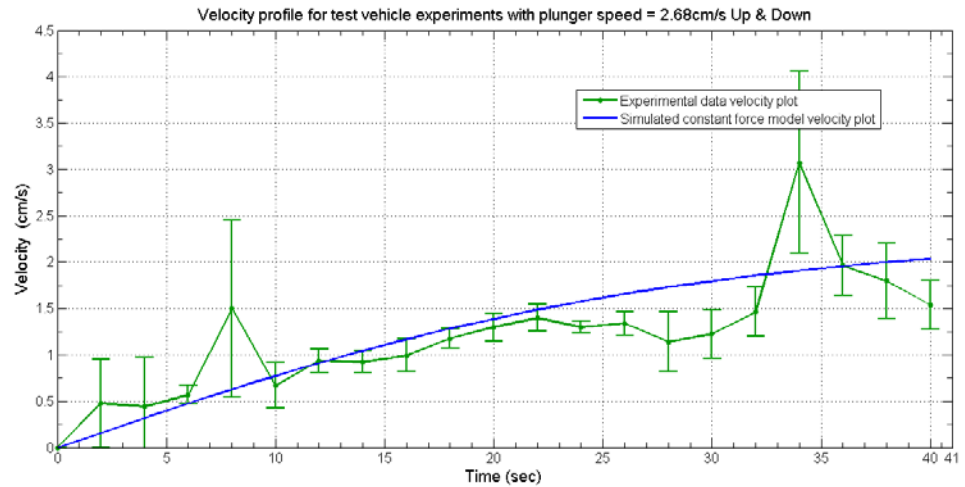


Figure 6.6 (f.2): Velocity plot: Plunger Speed = 2.68cm/s both Up and Down

## CASE 2 EXPERIMENTS

### Test Vehicle Position and Velocity profile curves: Showing the Constant Force Models

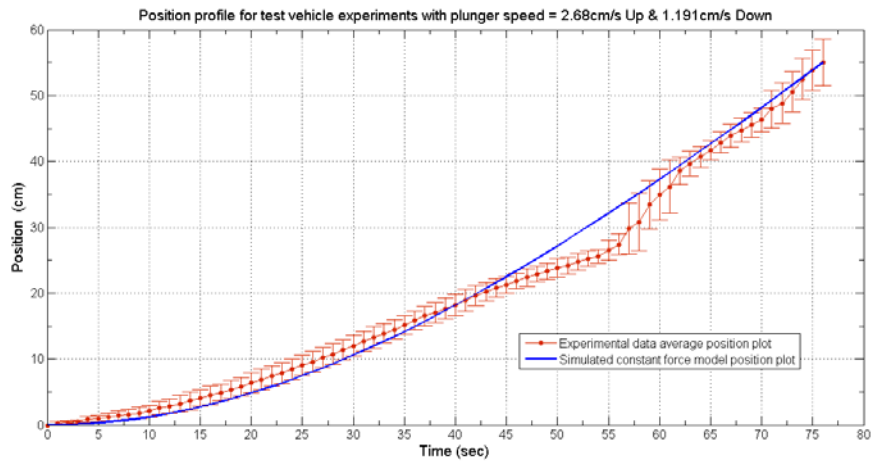


Figure 6.7 (a.1): Position plot: Plunger Speed = 2.68cm/s Up and 1.191cm/s Down

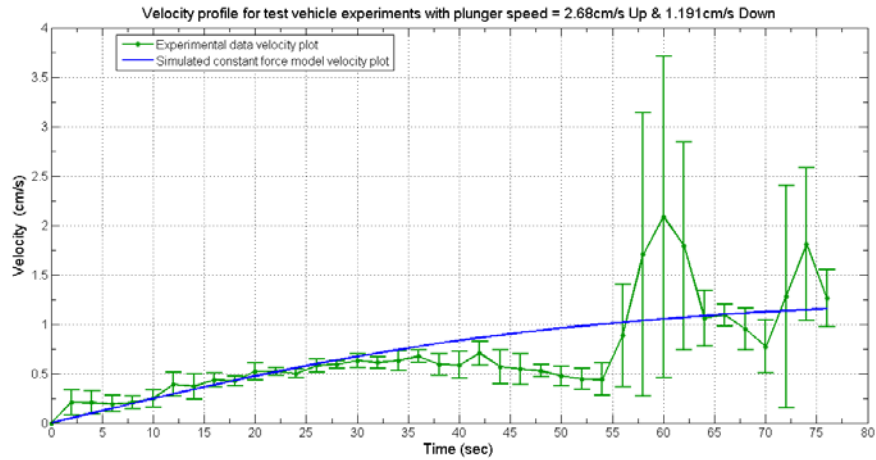


Figure 6.7 (a.2): Velocity plot: Plunger Speed = 2.68cm/s Up and 1.191cm/s Down

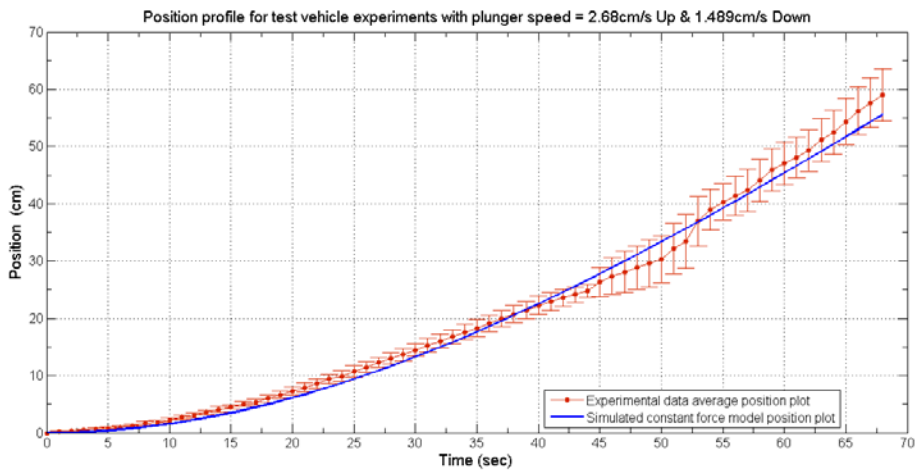


Figure 6.7 (b.1): Position plot: Plunger Speed = 2.68cm/s Up and 1.489cm/s Down

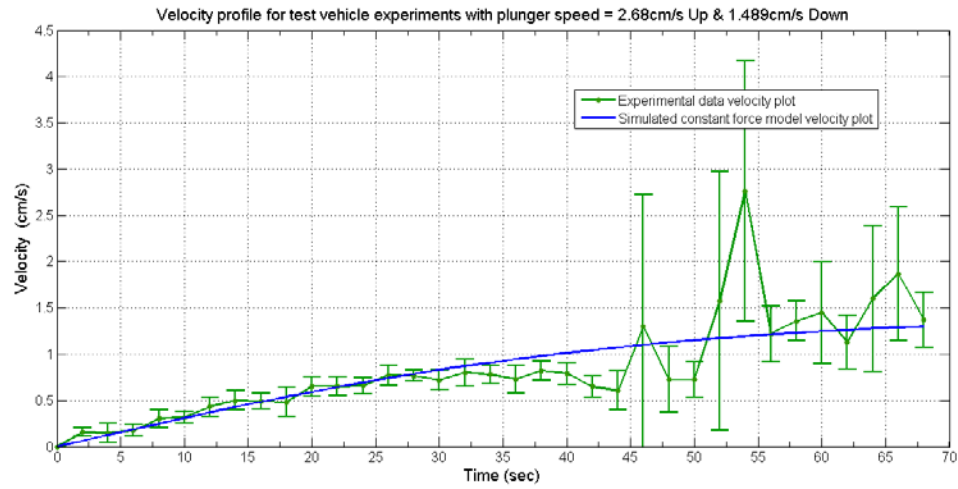


Figure 6.7 (b.2): Velocity plot: Plunger Speed = 2.68cm/s Up and 1.489cm/s Down

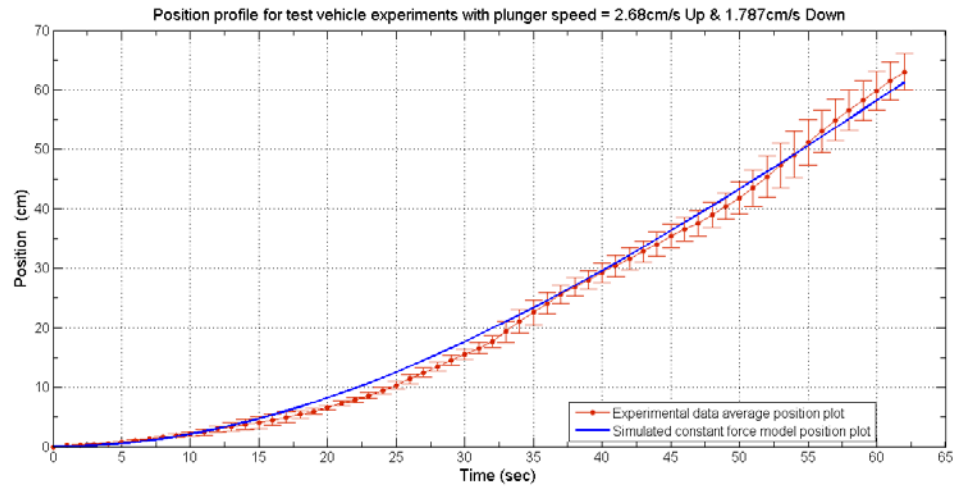


Figure 6.7 (c.1): Position plot: Plunger Speed = 2.68cm/s Up and 1.787cm/s Down

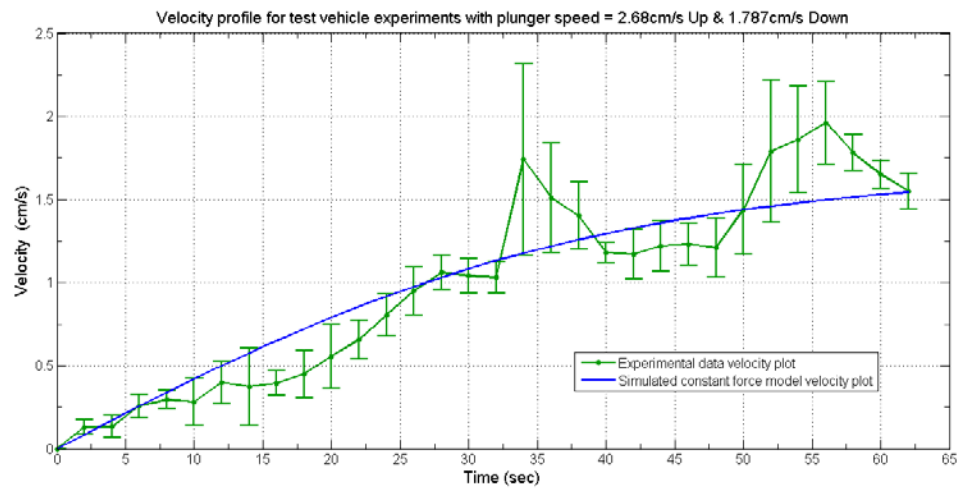


Figure 6.7 (c.2): Velocity plot: Plunger Speed = 2.68cm/s Up and 1.787cm/s Down

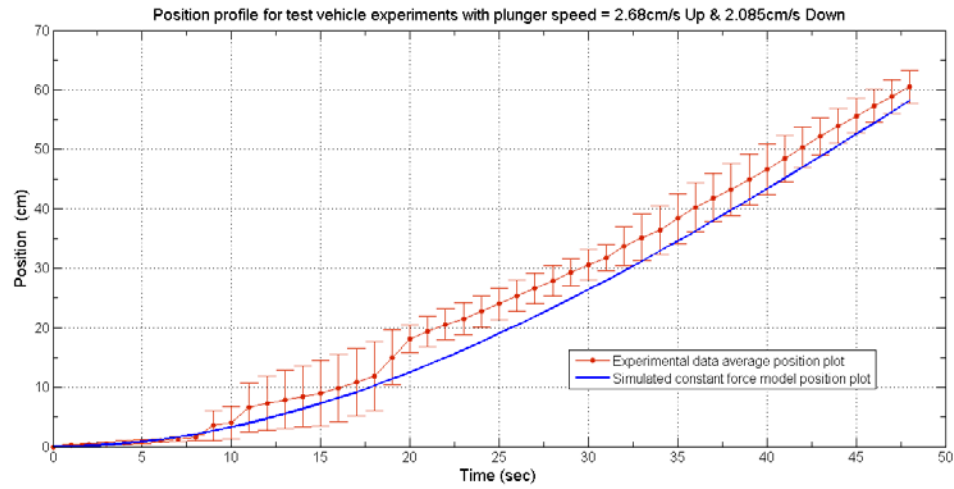


Figure 6.7 (d.1): Position plot: Plunger Speed = 2.68cm/s Up and 2.085cm/s Down

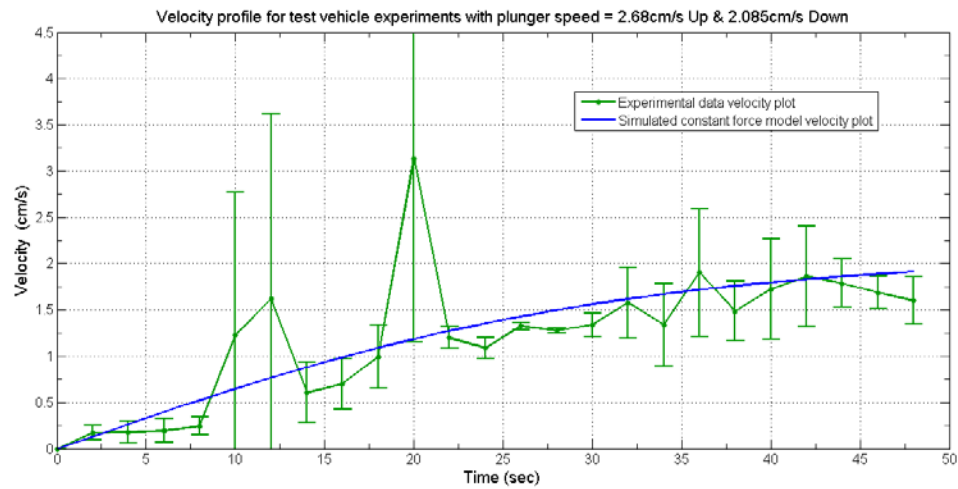


Figure 6.7 (d.2): Velocity plot: Plunger Speed = 2.68cm/s Up and 2.085cm/s Down

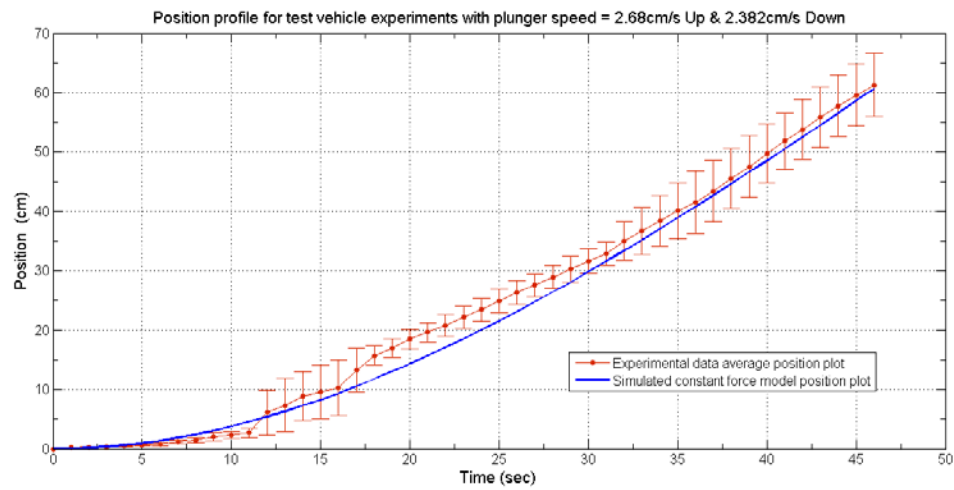


Figure 6.7 (e.1): Position plot: Plunger Speed = 2.68cm/s Up and 2.382cm/s Down



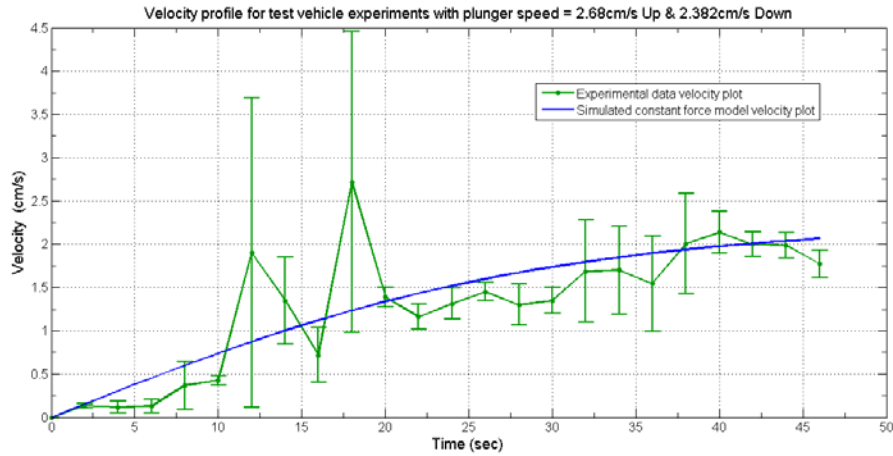


Figure 6.7 (e.2): Velocity plot: Plunger Speed = 2.68cm/s Up and 2.382cm/s Down

### CASE 3 EXPERIMENTS

#### Test Vehicle Position and Velocity profile curves: Showing the Constant Force Models

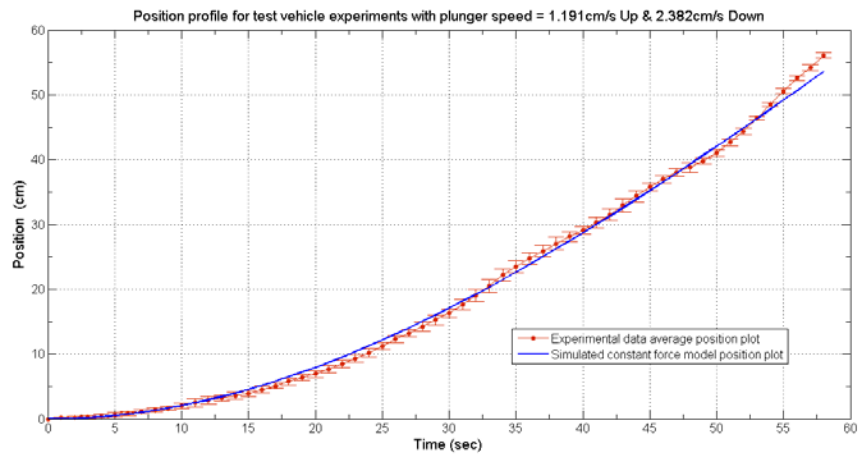


Figure 6.8 (a.1): Position plot: Plunger Speed = 1.191cm/s Up and 2.382cm/s Down

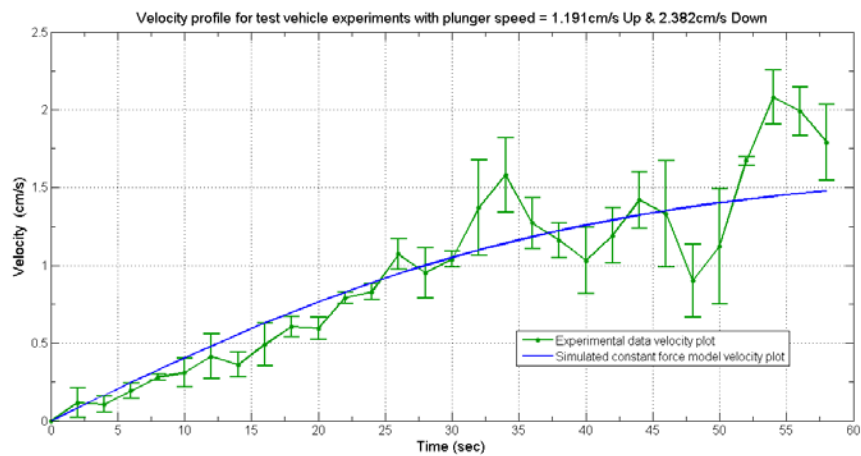


Figure 6.8 (a.2): Velocity plot: Plunger Speed = 1.191cm/s Up and 2.382cm/s Down



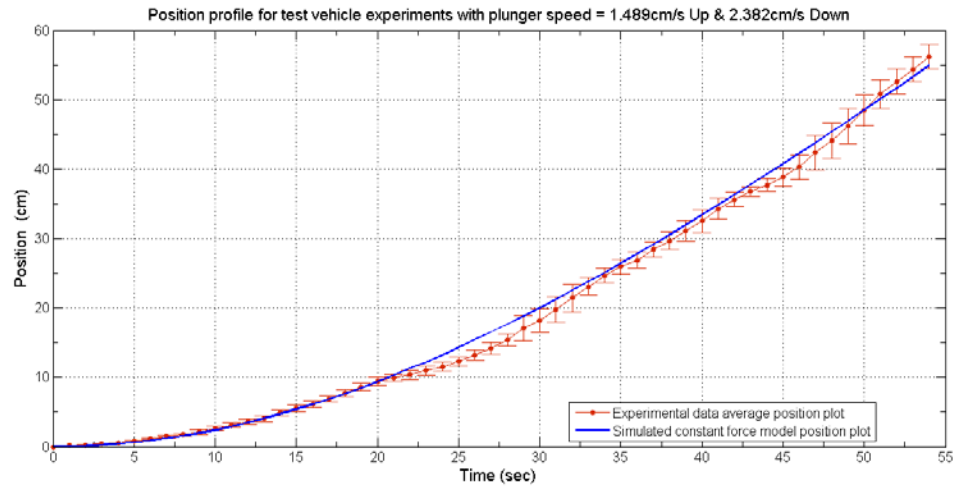


Figure 6.8 (b.1): Position plot: Plunger Speed = 1.489cm/s Up and 2.382cm/s Down

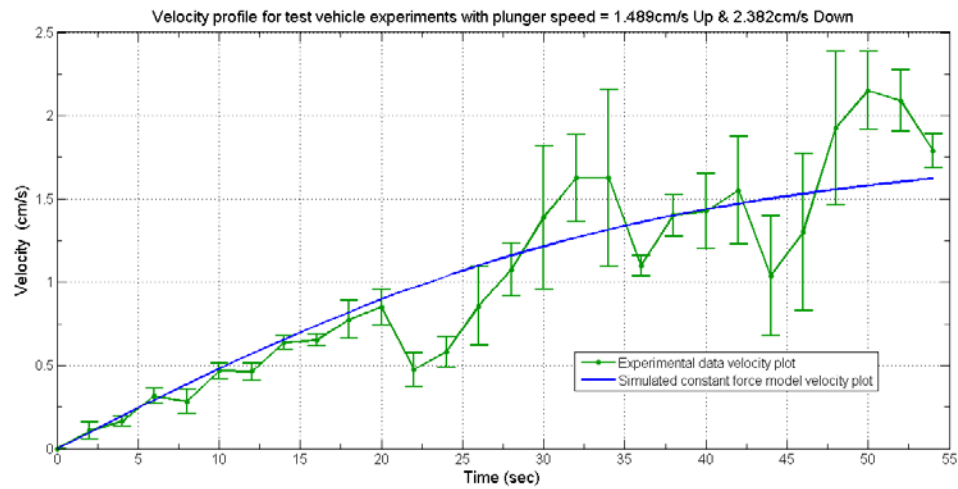


Figure 6.8 (b.2): Velocity plot: Plunger Speed = 1.489cm/s Up and 2.382cm/s Down

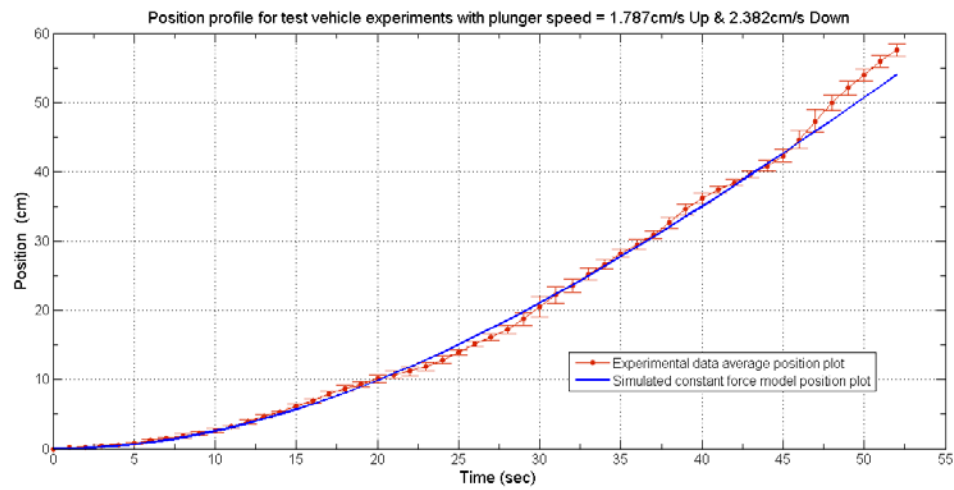


Figure 6.8 (c.1): Position plot: Plunger Speed = 1.787cm/s Up and 2.382cm/s Down

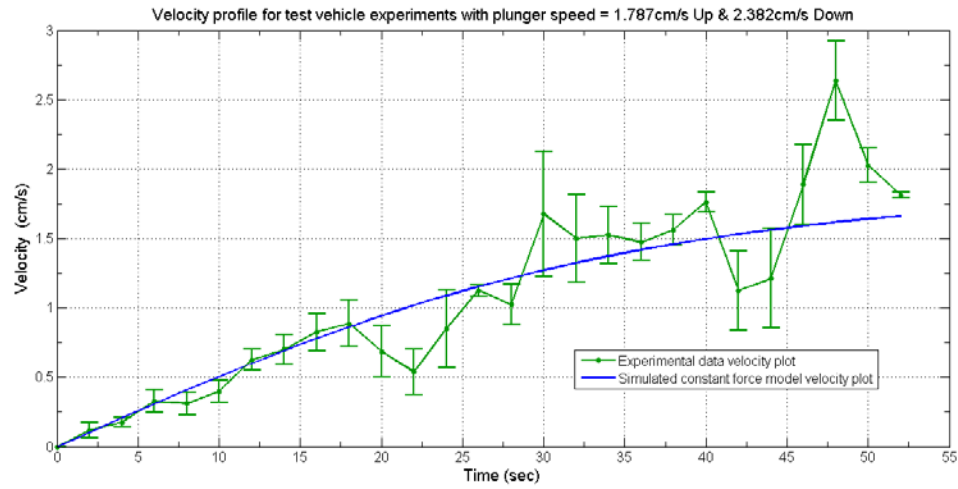


Figure 6.8 (c.2): Velocity plot: Plunger Speed = 1.787cm/s Up and 2.382cm/s Down

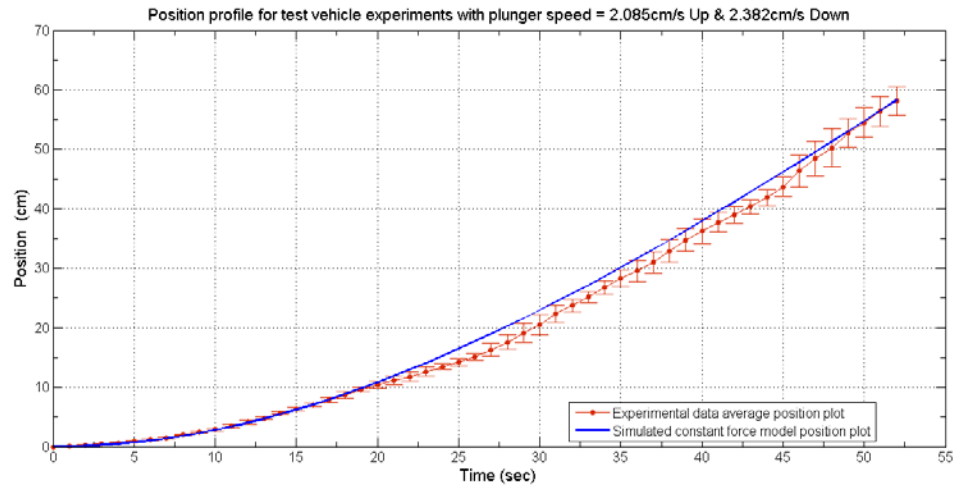


Figure 6.8 (d.1): Position plot: Plunger Speed = 2.085cm/s Up and 2.382cm/s Down

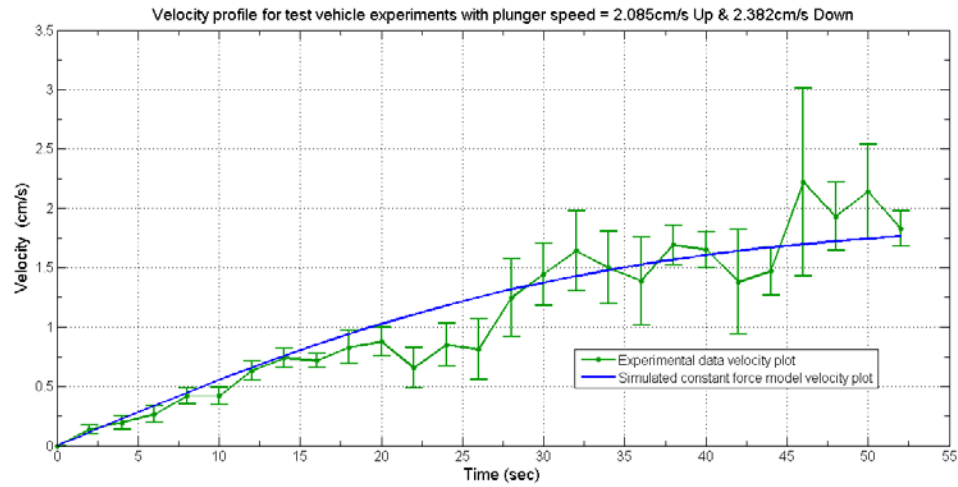


Figure 6.8 (d.2): Velocity plot: Plunger Speed = 2.085cm/s Up and 2.382cm/s Down

The vehicle speed comparison is done at 40s for all of the experiments since that is how long the fastest experiment ran before the actuator system was stopped. Both the thrust output and vehicle speed results for the CASE 3 experiments are normalized for a downstroke plunger velocity of 2.680cm/s. This is done by using Equations 3.2 and 3.3 to determine the difference in the theoretical thrust output for CASE 3 with a downstroke speed of 2.68cm/s instead of 2.382cm/s.

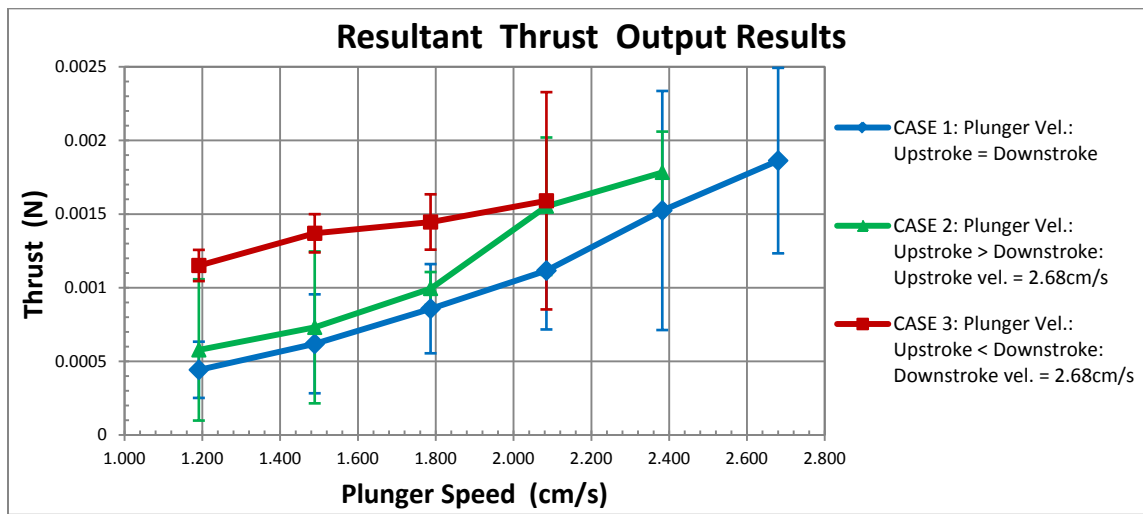


Figure 6.9(a): Resultant Constant Thrust Output Results

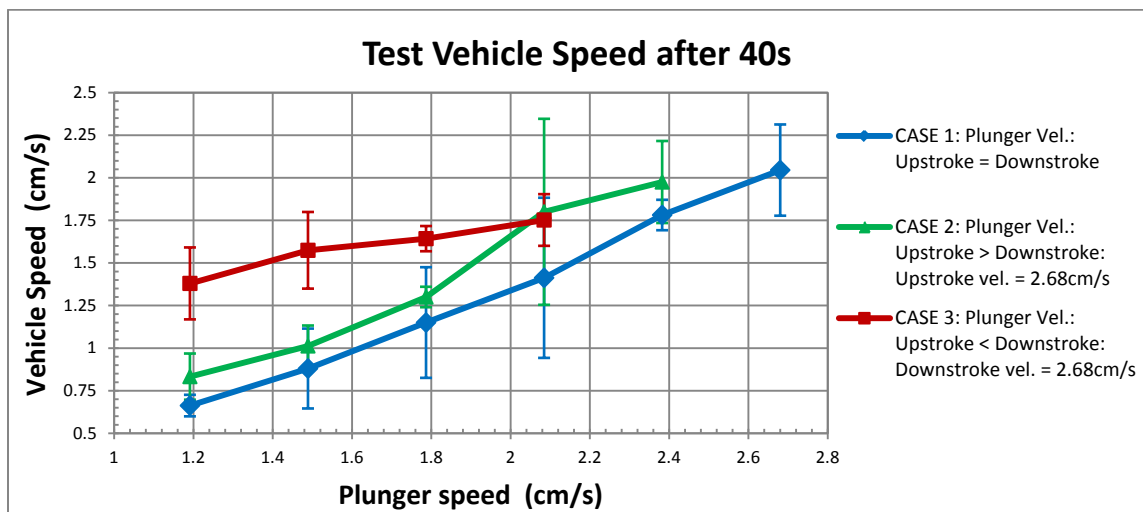


Figure 6.9(b): Vehicle Speed Results

The results presented in Figure 6.9(a) and Figure 6.9(b) show that for plunger speeds between 1.191cm/s and 2.085cm/s, higher propulsion forces and vehicle speeds can be achieved with actuation sequences where the plunger upstroke and downstroke speeds are different compared to those where both plunger strokes have equal speed. The time required for single cycles (one plunger upstroke and downstroke) for CASES 2 and 3 is less than that required for CASE 1 experiments (Table 6.1). Thus CASES 2 and 3 correspond to more plunger cycles at a time compared to CASE 1.

<b>Plunger Speed (cm/s)</b>	<b>Single Cycle time (sec): CASE 1</b>	<b>Single Cycle time (sec): CASES 2 and 3</b>
1.191	7.0000	5.1944
1.489	5.7000	4.5444
1.787	4.8333	4.1111
2.085	4.2143	3.8016
2.382	3.7500	3.5694
2.680	3.3889	

*Table 6.1: Cycle times for the various actuation cases.*

Additionally, the highest thrust output of the syringe-plunger propulsion mechanism and fastest test vehicle speeds are achieved with actuation sequences that have the plunger upstroke speed being slower than the downstroke speed (CASE 3). This can be attributed to smoother movement of the vehicle for these actuation sequences, Figure 6.1(c), which allows the vehicle to speed up faster and attain higher speeds. For the range of plunger speeds between 1.191cm/s and 2.085cm/s, the highest thrust output is 0.0016N and for this propulsive force the maximum speed attainable with the test vehicle used here is 2.13cm/s. Results are also presented for plunger speeds above

2.085cm/s and these show that even higher thrust output (0.0019N) is feasible. The corresponding maximum vehicle speed is 2.3cm/s.

While the above results are a good indication of the operation and viability of the syringe-plunger propulsion mechanism for small, low-speed, precision maneuvering underwater vehicles, there are various possible sources of error during testing. These include: vibrations due to the plunger movement in the syringe, the actuator direction change delay, valve switching (i.e. reaction forces due to spring back of the solenoids), non-uniformity of the flow of water into and out of the syringe, static friction of the rollers on the vehicle on the rails in the tank and ultrasonic distance sensor error/sensor reading error.

## **CHAPTER 7: CONCLUSIONS AND RECOMMENDATIONS**

In this chapter the results of this thesis are concluded and recommendations for future work are made based on the main experimental results presented in Section 3.4 and Section 6.1 and from the project as a whole.

### **7.1 CONCLUSIONS**

The core focus of this thesis is on the design and evaluation of a simple and low cost propulsion system prototype suitable for small, compact, low-speed maneuvering underwater vehicles. The primary contribution of this work has been the design of a propulsion system comprising primarily of a syringe and a plunger driven by a linear actuator that uses different intake and outflow nozzles to provide continuous propulsive force. The propulsion system provides low thrust, can enable low-speed maneuverability and allows for imbedding in the body of a vehicle for a smooth streamlined outer shape with no appendages.

The propulsion system design and the two main tests conducted to assess its viability are presented and discussed. First, thrust measurement experiments are done to determine the direct propulsive force output of the mechanism. It is shown that in the case of a single inflow and outflow orifice, the syringe-plunger system can provide much higher direct propulsive force in comparison to other functionally similar propulsion mechanisms presented in related research. In the case of different inflow and outflow

orifices it is found that the syringe-plunger system, though capable of providing continuous thrust has much lower net propulsive force output.

Next, a test vehicle is designed and built and the propulsion mechanism installed in it to facilitate testing, evaluation and modelling of the propulsive force output of the mechanism as well as the vehicle speed achievable by employing the propulsion system. Based on the experimental results and observations it is found that the syringe-plunger system is a viable propulsion mechanism for small, compact, low-speed underwater vehicles. It is capable of providing low enough continuous thrust to enable the low-speeds desirable for precision maneuvering and inspection tasks. Also, it is promising to know that even more thrust can be achieved through the combined use of a greater water/fluid control volume and faster plunger speeds.

Finally, through the design, assembly and testing course of this project it is found that though the proposed syringe-plunger propulsion mechanism is fairly simple in design, the overall experimentation process of the physical mechatronic system is rather complicated. However in retrospect, this provided valuable insight about the physical real-world system, its complexity and the challenges involved that could not have been discerned with simulation.

## **7.2 RECOMMENDATIONS FOR FUTURE WORK**

The design and analysis presented in this work for a propulsion mechanism for slow moving underwater vehicles can serve as a proof-of-concept for future research in the field of underwater robotics. It can also provide some useful insight into the areas of consideration and the challenges involved with underwater vehicles and systems research

for further work on AUVs at the University of Denver Unmanned Systems Research Institute (DU<sup>2</sup>SRI).

Several developments can be made to this research. First, Computational Fluid Dynamics (CFD) simulations, such as with ANSYS or ABAQUS CFD software, can be done to refine and validate the propulsion system and test vehicle design. This may result in faster design development and cost effectiveness. Second, design and implementation of a breakout PCB incorporating all the required connections can help provide easier access to the various parts of the apparatus by reducing the number of wires and make the system more versatile.

Also, the use of different, more flexible and robust actuators (e.g. pneumatic or hydraulic actuators) and sturdier valves may help minimize some of the mechanical and electrical failures and issues. Lastly, the design of a more streamlined and neutrally buoyant test vehicle with the propulsion system fully imbedded in it will better allow for implementation of multi-DOF maneuverability.



## REFERENCES

- [1] A. Mazumdar and H. H. Asada, "A compact underwater vehicle using high-bandwidth coanda-effect valves for low speed precision maneuvering in cluttered environments," in *2011 IEEE International Conference on Robotics and Automation*, pp. 1544–1550, 2011.
- [2] A. Thomas, M. Milano, M. G. G'Sell, K. Fischer, and J. Burdick, "Synthetic Jet Propulsion for Small Underwater Vehicles," in *Proceedings of the 2005 IEEE International Conference on Robotics and Automation*, pp. 181–187, April 2005.
- [3] P. Krishnamurthy, F. Khorrami, J. de Leeuw, M. E. Porter, K. Livingston, and J. H. Long, "A multi-body approach for 6DOF modeling of Biomimetic Autonomous Underwater Vehicles with simulation and experimental results," in *2009 IEEE International Conference on Control Applications*, pp. 1282–1287, 2009.
- [4] P. R. Bandyopadhyay, "Trends in biorobotic autonomous undersea vehicles," *IEEE J. Ocean. Eng.*, vol. 30, no. 1, pp. 109–139, Jan. 2005.
- [5] A. Mazumdar, M. Lozano, A. Fittery, and H. Harry Asada, "A compact, maneuverable, underwater robot for direct inspection of nuclear power piping systems," in *2012 IEEE International Conference on Robotics and Automation*, pp. 2818–2823, 2012.
- [6] F. Giorgio Serchi, A. Arienti, and C. Laschi, "Biomimetic Vortex Propulsion: Toward the New Paradigm of Soft Unmanned Underwater Vehicles," *IEEE/ASME Trans. Mechatronics*, vol. 18, no. 2, pp. 484–493, Apr. 2013.
- [7] X. Deng and S. Avadhanula, "Biomimetic Micro Underwater Vehicle with Oscillating Fin Propulsion: System Design and Force Measurement," in *Proceedings of the 2005 IEEE International Conference on Robotics and Automation*, pp. 3312–3317, April 2005.
- [8] D. Yoerger, J. G. Cooke, and J.-J. E. Slotine, "The influence of thruster dynamics on underwater vehicle behavior and their incorporation into control system design," *IEEE J. Ocean. Eng.*, vol. 15, no. 3, pp. 167–178, Jul. 1990.
- [9] A. Mazumdar and H. Asada, "Valve-PWM control of integrated pump-valve propulsion systems for highly maneuverable underwater vehicles," in *American Control Conference (ACC)*, pp. 5414–5420, 2012.

- [10] M. Krieg and K. Mohseni, "Thrust Characterization of a Bioinspired Vortex Ring Thruster for Locomotion of Underwater Robots," *IEEE J. Ocean. Eng.*, vol. 33, no. 2, pp. 123–132, Apr. 2008.
- [11] M. Krieg, A. Pitty, M. Salehi, and K. Mohseni, "Optimal Thrust Characteristics of a Synthetic Jet Actuator for Application in Low Speed Maneuvering of Underwater Vehicles," in *Proceedings of OCEANS 2005 MTS/IEEE*, pp. 1–6, 2005.
- [12] D. Brutzman, T. Healey, D. Marco, and B. McGhee, "The Phoenix autonomous underwater vehicle," *Artif. Intell. Mob. Robot. Case Stud. Success. Robot Syst.*, pp. 323–360, 1998.
- [13] D. Davis, "Precision maneuvering and control of the Phoenix Autonomous Underwater Vehicle for entering a recovery tube," Naval Postgraduate School, MONTEREY, CA, 1996.
- [14] R. B. Byrnes, A. J. Healey, R. B. McGhee, M. L. Nelson, S. Kwak, and D. P. Brutzman, "The Rational Behavior Software Architecture for Intelligent Ships," *Nav. Eng. J.*, vol. 108, no. 2, pp. 43–55, 1996.
- [15] D. Brutzman and M. Compton, "AUV Research at the Naval Postgraduate School," *Sea Technol. J.*, vol. 32, no. 12, pp. 35–40, 1991.
- [16] D. Marco, A. Healey, and R. McGhee, *Autonomous underwater vehicles: Hybrid control of mission and motion*. pp. 169–186, Springer US, 1996.
- [17] D. Brutzman, "A virtual world for an autonomous underwater vehicle," Naval Postgraduate School, MONTEREY, CA, 1994.
- [18] "Autonomous underwater vehicle - REMUS 100 - Kongsberg Maritime." [Online]. Available: <http://www.km.kongsberg.com/ks/web/nokbg0240.nsf/AllWeb/D241A2C835DF40B0C12574AB003EA6AB?OpenDocument>. [Accessed: 05-Feb-2014].
- [19] T. Furukawa, "Reactive obstacle avoidance for the remus autonomous underwater vehicle utilizing a forward looking sonar," Naval Postgraduate School, MONTEREY, CA, 2006.
- [20] A. Healey, "Obstacle avoidance while bottom following for the REMUS autonomous underwater vehicle," in *IFAC Symposium on Intelligent Autonomous Vehicles*, 2004.

- [21] D. Hemminger, “Vertical Plane Obstacle Avoidance and Control of the REMUS Autonomous Underwater Vehicle Using Forward Looking Sonar,” Naval Postgraduate School, MONTEREY, CA, 2005.
- [22] P. Patron, E. Miguelanez, Y. R. Petillot, D. M. Lane, and J. Salvi, “Adaptive mission plan diagnosis and repair for fault recovery in autonomous underwater vehicles,” in *OCEANS 2008*, pp. 1–9, 2008.
- [23] E. Miguelanez, P. Patron, K. E. Brown, Y. R. Petillot, and D. M. Lane, “Semantic Knowledge-Based Framework to Improve the Situation Awareness of Autonomous Underwater Vehicles,” *IEEE Trans. Knowl. Data Eng.*, vol. 23, no. 5, pp. 759–773, May 2011.
- [24] M. Sfakiotakis, D. M. Lane, and J. B. C. Davies, “Review of fish swimming modes for aquatic locomotion,” *IEEE J. Ocean. Eng.*, vol. 24, no. 2, pp. 237–252, Apr. 1999.
- [25] K. Mohseni, “Zero-mass Pulsatile Jets for Unmanned Underwater Vehicle Maneuvering,” in *AIAA 3rd “Unmanned Unlimited” Technical Conference, Workshop and Exhibit*, pp. 1–9, 2004.
- [26] E. Lee, “Design of a soft and autonomous biomimetic micro-robotic fish,” in *2010 5th IEEE Conference on Industrial Electronics and Applications*, pp. 240–247, 2010.
- [27] S. Tilley, “Smoothly does it,” *J. Exp. Biol.*, vol. 206, no. 4, 2003.
- [28] B. Smith and A. Glezer, “Vectoring and small-scale motions effected in free shear flows using synthetic jet actuators,” *AIAA Pap.*, vol. 213, 1997.
- [29] A. Glezer and M. Amitay, “Synthetic jets,” *Annu. Rev. Fluid Mech.*, vol. 34, no. 1, pp. 503–529, 2002.
- [30] A. Alexandrou, *Principles of fluid mechanics*, 4th ed. Prentice Hall, New Jersey, 2001.
- [31] F. . White, *Fluid Mechanics*, 7th ed. McGraw-Hill, New York, 2011.
- [32] W. Li and S. Lam, *Principles of fluid mechanics*. Addison-Wesley, Boston, MA, 1964.
- [33] J. Abbott, Z. Nagy, F. Beyeler, and B. J. Nelson, “Robotics in the Small, Part I: Microbotics,” *IEEE Robot. Autom. Mag.*, vol. 14, no. 2, pp. 92–103, Jun. 2007.

- [34] F. Beyeler, S. Muntwyler, and B. J. Nelson, “Design and calibration of a microfabricated 6-axis force-torque sensor for microrobotic applications,” in *2009 IEEE International Conference on Robotics and Automation*, pp. 520–525, 2009.
- [35] T. Prester, “Verification of a Six-Degree of Freedom Simulation Model for the REMUS Autonomous Underwater Vehicle,” MIT, 2001.
- [36] T. Prester, “Development of a six-degree of freedom simulation model for the REMUS autonomous underwater vehicle,” in *MTS/IEEE Oceans 2001. An Ocean Odyssey. Conference Proceedings (IEEE Cat. No.01CH37295)*, vol. 1, pp. 450–455, 2001.
- [37] J. Newman, *Marine hydrodynamics*. MIT Press, 1977.
- [38] F. Quagliotti, “Flight Mechanics,” pp. 72–76, 2012.
- [39] G. Martins, A. Moses, M. J. Rutherford, and K. P. Valavanis, “Enabling intelligent unmanned vehicles through XMOS Technology,” *J. Def. Model. Simul. Appl. Methodol. Technol.*, vol. 9, no. 1, pp. 71–82, Jan. 2011.
- [40] “XMOS, XK-1A Hardware Manual,” vol. REV 1.1.0, pp. 1–15, 2012.